

Large-Eddy Simulations of a Drizzling, Stratocumulus-Topped Marine Boundary Layer

ANDREW S. ACKERMAN *

NASA GODDARD INSTITUTE FOR SPACE STUDIES, NEW YORK

MARGREET C. VANZANTEN

ROYAL NETHERLANDS METEOROLOGICAL INSTITUTE
DE BILT, THE NETHERLANDS

BJORN STEVENS

DEPARTMENT OF ATMOSPHERIC AND OCEANIC SCIENCES
UNIVERSITY OF CALIFORNIA, LOS ANGELES, CALIFORNIA

VERICA SAVIC-JOVICIC

DEPARTMENT OF ATMOSPHERIC AND OCEANIC SCIENCES
UNIVERSITY OF CALIFORNIA, LOS ANGELES, CALIFORNIA

CHRISTOPHER S. BRETHERTON

DEPARTMENT OF ATMOSPHERIC SCIENCES
UNIVERSITY OF WASHINGTON, SEATTLE, WASHINGTON

ANDREAS CHLOND

MAX PLANCK INSTITUTE FOR METEOROLOGY
HAMBURG, GERMANY

JEAN-CHRISTOPHE GOLAZ

NOAA GEOPHYSICAL FLUID DYNAMICS LABORATORY
PRINCETON, NEW JERSEY

HONGLI JIANG

NOAA EARTH SYSTEM RESEARCH LABORATORY
BOULDER, COLORADO

MARAT KHAIROUTDINOV
SCHOOL OF MARINE AND ATMOSPHERIC SCIENCES
STONY BROOK UNIVERSITY, STONY BROOK, NEW YORK

STEVEN K. KRUEGER
DEPARTMENT OF METEOROLOGY
UNIVERSITY OF UTAH, SALT LAKE CITY, UTAH

DAVID C. LEWELLEN
MAE DEPARTMENT
WEST VIRGINIA UNIVERSITY, MORGANTOWN, WEST VIRGINIA

ADRIAN LOCK
MET OFFICE, EXETER, DEVON, UNITED KINGDOM

CHIN-HOH MOENG
NATIONAL CENTER FOR ATMOSPHERIC RESEARCH
BOULDER, COLORADO

KOZO NAKAMURA
JAMSTEC FRONTIER RESEARCH CENTER FOR GLOBAL CHANGE
YOKAHAMA CITY, KANAGAWA, JAPAN

MARKUS D. PETTERS
DEPARTMENT OF ATMOSPHERIC SCIENCE
COLORADO STATE UNIVERSITY, FORT COLLINS, COLORADO

JEFFERSON R. SNIDER
UNIVERSITY OF WYOMING, LARAMIE, WYOMING

SONJA WEINBRECHT
UNIVERSITY OF READING
READING, BERKSHIRE, UNITED KINGDOM

MIKE ZULAUF
DEPARTMENT OF METEOROLOGY
UNIVERSITY OF UTAH, SALT LAKE CITY, UTAH

* *Corresponding author address:* Andrew S. Ackerman, NASA Goddard Institute for Space Studies, New York, New York, 10025.
E-mail: andrew.ackerman@nasa.gov

ABSTRACT

Cloud-water sedimentation and drizzle in a stratocumulus-topped boundary layer are the focus of an intercomparison of large-eddy simulations. The context is an idealized case study of nocturnal stratocumulus under a dry inversion, with embedded pockets of heavily drizzling open cellular convection. Results from eleven groups are used. Two models resolve the size distributions of cloud particles, and the others parameterize cloud-water sedimentation and drizzle.

For the ensemble of simulations with drizzle and cloud-water sedimentation, the mean liquid water path (LWP) is remarkably steady and consistent with the measurements, the mean entrainment rate is at the low end of the measured range, and the ensemble-average maximum vertical wind variance is roughly half that measured. On average, precipitation at the surface and at cloud base is smaller, and the rate of precipitation evaporation greater, than measured. The vertical gradient of moisture correlates well with LWP but not with precipitation. LWP is well-correlated with the ratio of radiative cooling to the sum of entrainment warming plus latent heating associated with precipitation, a correlation largely determined by model dynamics. LWP is also influenced by microphysics, decreasing as the propensity for drizzle is increased. Including cloud-water sedimentation in the simulations always decreases entrainment substantially and increases LWP. In contrast, LWP nearly always decreases in response to including drizzle. In all but a few cases cloud-water sedimentation dominates the LWP response to drizzle. The omission of cloud-water sedimentation in simulations is strongly discouraged, even for clouds not precipitating below cloud base.

1. Introduction

Marine boundary-layer clouds cover vast areas of the global ocean and exert a substantial shortwave radiative forcing on the global heat budget (Klein and Hartmann 1993). Evidence suggests they constitute a leading-order uncertainty in cloud feedbacks in global climate models (Bony and Dufresne 2005), largely attributable to difficulties in representing them in large-scale models. The GCSS (GEWEX (Global Energy and Water Exchange) Cloud System Study) project was developed to improve cloud parameterizations in climate and numerical weather prediction models (Randall et al. 2003). The GCSS Boundary Layer Cloud Working Group (BLCWG) has conducted a number of workshops devoted to idealized case studies of low-lying clouds simulated with a range of models. The preceding BLCWG inter-comparison of large-eddy simulations (LES) concerned the first research flight of DYCOMS-II (the second Dynamics and Chemistry of Marine Stratocumulus Field Study), in which very dry air overlay a stratocumulus-topped marine boundary layer, with average cloud droplet concentrations of about 100 cm^{-3} and no measurable precipitation below cloud base (Stevens et al. 2005b). Models that reduced subgrid-scale mixing at cloud top were found best able to maintain sufficient radiative cooling while concurrently limiting entrainment at cloud top, resulting in a well-mixed boundary layer topped by an optically thick cloud layer, as observed. Cloud-water sedimentation and drizzle were ignored in the simulations, which is a traditional approach in studies of non-precipitating clouds.

A number of investigations over the years have considered the effects of drizzle on the stratocumulus-topped boundary layer, and here we scratch the surface of that literature. Brost et al. (1982) and Nicholls (1984) made in situ measurements and found drizzle fluxes comparable to turbulent moisture fluxes. Brost et al. (1982) suggested that the combination of latent heating in the cloud and cooling below can stabilize the boundary layer and thereby decouple the cloud from the sub-cloud layer. Nicholls (1984) confirmed this idea with a simple model and furthermore found that drizzle reduces entrainment of overlying air by the boundary layer. From analysis of other in situ measurements, Paluch and Lenschow (1991)

proposed a conceptual model in which drizzle-induced decoupling leads to heat and moisture accumulating below cloud, generating convective instability that is relieved by cumuliform convection, which breaks up a stratiform cloud layer. With a numerical model Ackerman et al. (1993) found that positive feedback between drizzle and cloud condensation nuclei concentrations can result in a boundary layer being unable to sustain the radiative cooling that drives convection and maintains its depth in the presence of large-scale subsidence.

Stevens et al. (1998) used LES with bin microphysics to show that heavy drizzle ($\sim 1 \text{ mm d}^{-1}$ at the surface) not only stabilizes the cloud layer with respect to the sub-cloud layer but also dries out the downdrafts such that they become buoyant above mean cloud base, thereby diminishing the generation of turbulence kinetic energy. The delayed downdraft buoyancy induced by the sedimentation flux divergence at cloud top, not realized until all the condensed water evaporates above mean cloud base, is described as “potential buoyancy” by Stevens et al. (1998). In that study, liquid water path (LWP) was found to be dramatically reduced by heavy drizzle, owing to the surface moisture sink of precipitation and reduced mixing between the cloud and sub-cloud layers¹. Stevens et al. (1998) also found entrainment to decrease in the presence of heavy drizzle. Though with little difference between the humidity above and within the boundary layer, there was little effect of the reduced entrainment on boundary-layer moisture in their simulations.

Related to concerns regarding boundary-layer dynamics, there is considerable climate-related interest in so-called indirect aerosol effects (radiative forcings induced by changes in aerosol concentrations through modification of cloud properties). As recognized by Twomey (1974), increased aerosol concentrations can enhance cloud-droplet concentrations, and distributing a fixed amount of water over more – and thus smaller – droplets results in more reflective clouds, which results in a negative radiative forcing. But smaller droplets also produce drizzle less efficiently, and a number of studies have shown that decreased drizzle

¹Although the boundary layer is not well-mixed in such a scenario, the cumuliform convection that develops does couple the cloud and sub-cloud layers, leading Stevens et al. (1998) to comment that “decoupling” is a carelessly used term in the literature, which we perpetuate here.

can lead to thicker clouds with more condensed water (e.g., Albrecht 1989; Pincus and Baker 1994), thereby reflecting even more sunlight.

Despite expectations of decreased drizzle leading to increased cloud water, measurements of ship tracks – aerosol plumes within marine stratocumulus cloud decks – indicate that cloud water tends to decrease, if anything, rather than increase in clouds with higher droplet concentrations (Ackerman et al. 2000; Platnick et al. 2000; Coakley and Walsh 2002). A possible explanation is provided by a modeling study (Ackerman et al. 2004) that showed LWP increasing with droplet concentrations only when sufficient drizzle reaches the surface (more than $\sim 0.1 \text{ mm d}^{-1}$), a condition favored by moist air overlying the boundary layer. Otherwise, reductions in drizzle (or even in just cloud-water sedimentation) induced by increasing droplet concentrations were found instead to reduce LWP by increasing entrainment of dry air from aloft. The potential buoyancy mechanism of Stevens et al. (1998) was suggested as the mechanism underlying the decrease in entrainment with increasing droplet concentrations. However, Bretherton et al. (2007), who also found that decreasing cloud-water sedimentation can reduce LWP, argued that the potential buoyancy concept does not apply to cloud-water sedimentation, and that diminished entrainment results instead from a sedimentation-induced reduction in the evaporative cooling available to promote mixing at cloud top.

Notwithstanding the likelihood that drizzle can strongly affect boundary-layer dynamics, it may not be the predominant cause of decoupling in cloud-topped boundary layers, as there is a substantial body of theoretical work showing that such decoupling can arise from the dynamics of deepening boundary layers independent of drizzle (e.g., Krueger et al. 1995a; Bretherton and Wyant 1997; Stevens 2000; Lewellen and Lewellen 2002). Nonetheless, here we focus on the effects of drizzle and cloud-water sedimentation on the dynamics and bulk properties of a stratocumulus-topped marine boundary-layer, through simulations based on an idealization of a cloud deck with patchy drizzle. Another aim is to evaluate how well an assortment of LES models are able to match observed cloud properties, precipitation, and

dynamics. We note that the BLCWG has also compared single-column models using the same specifications developed for this study, as described by Wyant et al. (2007).

2. Setup of Simulations

The specifications for the simulation intercomparison are based on an idealization of nocturnal aircraft measurements obtained during the second research flight (RF02) of DYCOMS-II (Stevens et al. 2003a). The cloud field sampled on that flight was bimodal, with pockets of heavily drizzling open cells amidst a deck of closed-cell stratocumulus that was drizzling lightly (vanZanten and Stevens 2005; Stevens et al. 2005a). These two populations not only had different rates of precipitation, but their aerosol distributions were also notably different (Petters et al. 2006). For the intercomparison, the initial thermodynamic conditions represent an average over these two cloud populations, while the prescribed microphysical conditions represent an average over the open cells. The latter is an ad hoc modification made after the workshop (at the 2005 pan-GCSS meeting in Athens, Greece) to compensate for the greatest domain-average surface precipitation in the preliminary simulation ensemble being about half that observed. In stratocumulus the precipitation rate at cloud base is not expected to be a linear function of liquid water path (e.g., Pawlowska and Brenguier 2003; Comstock et al. 2004; vanZanten et al. 2005), so even if the models and measurements were perfect the average thermodynamic and microphysical conditions would not be expected to produce a simulated cloud field that matches the measurement average. Because of this fundamental problem, here we consider the trends among the model simulations as much if not more so than the comparisons between simulations and measurements.

a. Initial Conditions

The initial atmospheric profiles of wind, moisture, and temperature were composited from the horizontally averaged measurements as

$$u = 3 + 4.3z/1000 \text{ m s}^{-1} \quad (1)$$

$$v = -9 + 5.6z/1000 \text{ m s}^{-1} \quad (2)$$

$$q_t = \begin{cases} 9.45 \text{ g kg}^{-1} & z < z_i \\ 5 - 3[1 - \exp([z - z_i]/500)] \text{ g kg}^{-1} & \text{otherwise} \end{cases} \quad (3)$$

$$\theta_l = \begin{cases} 288.3 \text{ K} & z < z_i \\ 295 + (z - z_i)^{1/3} \text{ K} & \text{otherwise} \end{cases} \quad (4)$$

where u and v are westerly and southerly winds, z is altitude in m, z_i the initial inversion height of 795 m, q_t the total water mixing ratio (sum of the mass mixing ratios of water vapor, q_v , and liquid water, q_l), and θ_l a linearized liquid-water potential temperature:

$$\theta_l = (p_{\text{ref}}/p)^{R_d/c_p}(T - Lq_l/c_p)$$

in which p and T are atmospheric pressure and temperature, $p_{\text{ref}} = 1000 \text{ mb}$, $R_d = 287 \text{ J kg}^{-1} \text{ K}^{-1}$, $c_p = 1004 \text{ J kg}^{-1} \text{ K}^{-1}$, and $L = 2.5 \text{ MJ kg}^{-1}$. Surface pressure is assumed to be constant at 1017.8 hPa. To accelerate the spin-up of convection, it was recommended to pseudo-randomly perturb the initial temperatures within the boundary layer about their horizontal means with an amplitude of 0.1 K, and to initialize the turbulence kinetic energy (TKE) in models with prognostic subgrid-scale schemes at $1 \text{ m}^2 \text{ s}^{-2}$.

For comparison with the previous BLCWG case, RF01 of DYCOMS-II, we note that the air above the inversion is moister and cooler here, and both differences are conducive to drizzle. For a 50-m thick inversion layer the initial jumps in q_t and θ_l in the present case are 4.7 g kg^{-1} and 10.4 K, compared to 7.5 g kg^{-1} and 12.2 K in Stevens et al. (2005b). Thus, while the previous case was unstable with respect to the classic cloud-top entrainment instability threshold (Deardorff 1980a; Randall 1980), the present case is not.

b. Forcings

As in previous BLCWG stratocumulus cases, no large-scale horizontal flux divergences of θ_l or q_t are considered; thus the conceptual framework is of a model grid advecting with the mean wind, in which there is no change in the imposed boundary conditions over the duration of the simulation. Other than surface boundary conditions, all of the forcings are identical to those in Stevens et al. (2005b). Uniform divergence of the large-scale horizontal winds: $D = 3.75 \times 10^{-6} \text{ s}^{-1}$ is assumed, chosen so that subsidence warming above the inversion balances the derived radiative cooling there. The large-scale vertical wind is computed as $w_{\text{LS}} = -Dz$ and appears as a source term for each prognostic variable ϕ as $w_{\text{LS}}\partial\phi/\partial z$. A large-scale horizontal pressure gradient is included in the u and v equations by assuming that the geostrophic wind is given by the initial wind profile at a latitude of 31.5°N . Radiative heating rates are computed every time step from the divergence of a longwave radiative flux profile in each model column using the parameterization from Stevens et al. (2005b):

$$F(z) = F_0 \exp[-Q(z, \infty)] + F_1 \exp[-Q(0, z)] + a\rho_i c_p D H(z - z_i) [0.25(z - z_i)^{4/3} + z_i(z - z_i)^{1/3}] \quad (5)$$

where

$$Q(z_1, z_2) = \int_{z_1}^{z_2} \kappa \rho q_l dz \quad (6)$$

in which $a = 1 \text{ K m}^{-1/3}$, ρ is air density, $\rho_i = 1.12 \text{ g m}^{-3}$ (air density at initial z_i), H is the Heaviside step function, z_i is defined throughout as the lowermost altitude where $q_t = 8 \text{ g kg}^{-1}$, and $F_0 = 70 \text{ W m}^{-2}$, $F_1 = 22 \text{ W m}^{-2}$, and $\kappa = 85 \text{ m}^2 \text{ kg}^{-1}$. Theoretical justification for this parameterization is provided by Larson et al. (2007), where its range of applicability (which includes the conditions considered here) is discussed.

The only forcings that depart from Stevens et al. (2005b) are the surface boundary conditions, here taken from the measurements of vanZanten and Stevens (2005) and designed to minimize departures from the measurements while allowing the evolving wind field to feed back on the surface momentum fluxes. Upward sensible and latent heat fluxes, apart from

any precipitation flux, are fixed at the measured averages of 16 and 93 W m⁻², respectively, in which a surface air density of 1.21 kg m⁻³ is implicit. The upward surface momentum flux is computed as $-u_i u_\star^2 / |U|$, where wind components u_i and magnitude $|U|$ are defined locally and the friction velocity is fixed at $u_\star = 0.25$ m s⁻¹. The latter was obtained from preliminary simulations using surface-similarity boundary conditions.

c. Cloud Microphysics

For models that prescribe the number concentration of cloud droplets (N_d) a uniform value of $N_d = 55$ cm⁻³ was specified, based on averages over horizontal flight legs within the open cells (see Table 1). For models with bin microphysics, an idealized, uniform aerosol distribution was derived from measurements, as described in Appendix A. Models with bin microphysics are initialized without water droplets, implying an incipient cloud layer that is initially supersaturated. Activating large numbers of Aitken-mode particles during convection spin-up would hamper precipitation development relative to models that fix N_d . To avoid such an undesirable course, the maximum supersaturation used for droplet activation is limited to 1% during the first hour, resulting in activation of ~ 70 cm⁻³ droplets during that time. This limit is applied to droplet activation only, and not to condensational growth.

Bin microphysics models automatically treat sedimentation of cloud droplets, unlike other models that typically ignore the process. For those models cloud-water sedimentation is included here by assuming a log-normal size distribution of droplets falling in a Stokes regime, in which the sedimentation flux is given by

$$F = c [3/(4\pi\rho_l N_d)]^{2/3} (\rho q_c)^{5/3} \exp(5 \log^2 \sigma_g) \quad (7)$$

where $c = 1.19 \times 10^8$ m⁻¹ s⁻¹ (Rogers 1979), ρ_l is the density of liquid water, q_c the mixing ratio of cloud water, and σ_g the geometric standard deviation of the size distribution. A value of $\sigma_g = 1.5$ was specified, based on the mean value mean minus one standard deviation of $(\overline{r^2})^3 / (\overline{r^3})^2$ (where r is droplet radius) reported by Martin et al. (1994) for stratocumulus in continental airmasses. In retrospect, a value of $\sigma_g = 1.2$ would have been more consistent

with the cloud-droplet size distributions measured during RF02, as well as being closer to the maritime average found by Martin et al. (1994). This smaller value, corresponding to a narrower size distribution, is considered in a sensitivity test.

3. Results

Beyond the results and analyses presented here, a complete set of the submitted model results is available at the GCSS DIME (Data Integration for Model Evaluation) website (<http://gcss-dime.giss.nasa.gov>). The models are described and the output variables defined in Appendices B and C, respectively. Time series are interpolated to a uniform temporal grid with 300-s spacing; profiles are interpolated to a uniform vertical grid with 2-m spacing.

a. Domain Averages

After two hours of simulation with drizzle and cloud-water sedimentation included, the transient spin-up of boundary-layer convection has completed, and the simulation ensemble settles into a pseudo-steady state in which properties such as LWP, entrainment, precipitation, and the maximum of vertical wind variance ($\overline{w'^2}$) are nearly constant, as seen in Fig. 1. The middle half (middle two quartiles) of the ensemble characterizes the range of LWP estimated from the measurements remarkably well, and the full range of the ensemble is nearly twice again as broad. The entrainment rate in the simulations is computed here as $dz_i/dt + Dz_i$, and the ensemble is roughly centered on the low end of the measured range (derived from conservative tracers). The boundary layer is deepening in all the simulations, with a mean entrainment rate about twice the subsidence rate at the initial z_i , and thus none of the simulated boundary layers are in a true steady-state. While agreement of the ensemble LWP and entrainment rate with measurements is favorable, further comparisons tend to be less so. For instance, the intensity of convection given by the maximum $\overline{w'^2}$ is about half that measured. As shown below, the measurements suggest a well-mixed boundary layer,

but a number of aspects of the simulations suggest some decoupling.

The ensemble range of domain-mean precipitation rates at the surface is substantial and the distribution is skewed, with the mean corresponding roughly to the lower end of the measured average and the median about half that (Fig. 1). At cloud base, the simulated precipitation varies widely among the simulations (Fig. 2). On the one hand, precipitation at cloud base and at the surface in more than half the simulations is substantially less than that measured. On the other hand, the results in a majority of simulations fall within $\pm 50\%$ of the combined measurements of LWP and cloud-base precipitation. And while the fractional loss of precipitation below cloud base in most of the simulations exceeds that in the measurements, all the simulations fall within $\pm 50\%$ of the combined measurements of LWP and fractional precipitation loss. Greater loss of precipitation below cloud base is observed when stratocumulus drizzle is less intense (vanZanten et al. 2005), consistent with the overall differences between the simulations and observations here. Correlations between LWP and precipitation are weak, though for both models that vary the propensity of precipitation (DHARMA and UCLA), LWP falls as the propensity increases and precipitation at the surface and at cloud base rises, while the fractional loss decreases. No clustering systematically related to microphysics schemes is evident, as results from the most complex methods (bin models of DHARMA and RAMS) and those from the simplest (single-moment schemes of NHM and Utah) are interspersed with those from the rest of the models, which use double-moment schemes. As shown below, inter-model differences in microphysics schemes are generally dominated by differences in model dynamics.

Also seen in Fig. 2, the majority of simulations produce a fairly solid cloud deck, with cloud cover greater than 95% for all but two of the simulations. No integral measure of cloud cover is available for comparison.

The impacts of cloud-water sedimentation are substantial, as found elsewhere (Ackerman et al. 2004; Bretherton et al. 2007). Compared to the ensemble means with cloud-water sedimentation omitted, including it reduces entrainment by $\sim 25\%$ (Fig. 1). The diminished

entrainment results in a cooler, moister boundary layer, with ensemble mean LWP increasing by $\sim 20\%$ and surface precipitation increasing roughly fourfold. As discussed further below, the maximum $\overline{w'^2}$ decreases by $\sim 10\%$.

b. Profiles

Excluding the scatter above the inversion layer, the ensemble distributions of θ_l and q_t are tight (Fig. 3), with the observed θ_l profile well matched by the simulations while the gradient in the simulated q_t profiles indicates a somewhat less well-mixed boundary layer than observed. Comparatively broader ensemble distributions are seen in all the other profiles, with the middle half of the distribution reproducing not only the observed q_t but also the cloud fraction profile remarkably well.

The ensemble distribution of precipitation is even broader, and the middle half of the distribution falls between that measured in closed and open cells. The difference between closed and open cells is prominent in the precipitation measurements. The precipitation flux in the middle half of the ensemble is closer to that in the open cell measurements in the upper region of the cloud, and transitions to values closer to the closed cell measurements at lower elevations. The skewness of the ensemble distribution is only evident below the cloud layer. The effect of cloud-water sedimentation on precipitation is seen to be profound throughout the ensemble profile, and the differences increase with height. As might be expected in a lightly drizzling regime, the shape of the precipitation profile is dominated by cloud-water sedimentation, and thus peaks near cloud top rather than near cloud base as found in heavily drizzling stratocumulus, both in measurements (e.g., Nicholls 1984) and in simulations (e.g., Ackerman et al. 2004). As noted by vanZanten and Stevens (2005), it may not be possible to composite a representative profile from in situ measurements for the present case, as measured precipitation rates are small near cloud base, possibly because open cells were poorly sampled at that flight level; radar observations, however, indicate that precipitation was likely greatest near cloud base in the open cells.

The total fluxes of θ_l and q_t in Fig. 3 include not only advective and subgrid-scale fluxes but also precipitation, and in the case of θ_l , radiation as well; fluxes associated with large-scale subsidence are neglected. The spread in the ensemble is substantial, as are the differences between closed and open cells. The middle half of the ensemble resembles the observations in closed cells more than in open cells, except for the q_t flux in the upper region of the cloud, reminiscent of precipitation. Beyond that exception, the ensemble does not envelop the total fluxes measured in the open cells, consistent with the underprediction of precipitation below cloud. To the degree that the mean profiles of these total fluxes are linear within the boundary layer, they are consistent with a quasi-steady state boundary layer in which the shapes of the θ_l and q_t profiles are steady, since the divergence of a linear flux profile is independent of height. Consistent with the evolution of the θ_l and q_t profiles, the gradient of the ensemble mean θ_l flux implies a boundary layer that is warming, and the lack of gradient in the mean q_t flux implies a boundary layer neither drying nor moistening on average, though there is a hint of an implied drying tendency approaching cloud top.

The middle half of the buoyancy flux distribution is more consistent with the measurements in the closed cells within the cloud, but closer to the measurements in the open cells just below cloud, which is essentially the opposite relationship between simulated and observed precipitation fluxes with respect to open and closed cells. (For brevity we refer to buoyant production of TKE throughout as a buoyancy flux, though it is actually a buoyancy flux times g/ρ , where $g = 9.8 \text{ m s}^{-2}$.) Only in the lower quartile of the ensemble are the time-averaged buoyancy fluxes negative below cloud base, a condition associated with decoupling between the cloud and sub-cloud layers (e.g., Nicholls 1984; Turton and Nicholls 1987).

The $\overline{w'^2}$ measurements suggest profiles with a single peak near the middle of the boundary layer. This shape is characteristic of well-mixed boundary layers and is unlike the simulation ensemble, in which $\overline{w'^2}$ peaks within the cloud layer and levels off below cloud base. The large values measured at mid-levels are well beyond the ensemble range, further suggesting

a less convectively mixed boundary layer in the simulations. Stevens et al. (2005b) found a similar result. We note that the $\overline{w'^2}$ measurements include contributions at scales larger than the 6.4-km wide model domain, with measurements indicating spectral power of order 10% of the total at greater scales (Petters et al. 2006).

In the final panel of Fig. 3 it is seen that measured vertical winds are negatively skewed just above cloud base, with downdrafts stronger than updrafts. In contrast, vertical winds are skewed positively in the simulations, consistent with more cumuliform convection. Omitting cloud-water sedimentation results in $\overline{w'^3}$ substantially decreased through much of the cloud layer, as discussed further below.

c. Trends Within Ensemble

As background, recall that in the non-precipitating stratocumulus simulations of Stevens et al. (2005b), the vertical gradient of q_t within the boundary layer was inversely correlated with both the maximum $\overline{w'^2}$ and the minimum buoyancy flux near cloud base, consistent with negative buoyancy fluxes being associated with boundary-layer decoupling. It was also found that the trend between simulations in the ratio of entrainment warming to radiative cooling was inversely proportional to LWP. That is, simulations that entrained more efficiently relative to radiative cooling produced drier cloud layers.

First we consider relationships in the ensemble between three quantities associated with decoupling: (i) maximum $\overline{w'^2}$, (ii) minimum buoyancy flux between 150 and 750 m altitude, and (iii) δq_t , the difference in q_t between averages over altitude ranges of 650–750 m and 50–150 m. Similar to the findings of Stevens et al. (2005b), δq_t is seen in Fig. 4 to be inversely correlated with maximum $\overline{w'^2}$, consistent with convective intensity being conducive to a well-mixed boundary layer. Unlike in Stevens et al. (2005b), here δq_t does not correlate well with the minimum buoyancy flux (not shown) though the two are well-correlated in the absence of drizzle (also not shown). Note that these statistics are first obtained from half-hourly profiles and then averaged over the last four hours, a method that results in more

instances of negative minimum buoyancy fluxes than might be construed from Fig. 3.

If evaporation of drizzle led to decoupling in the simulations, one might expect δq_t to increase with precipitation at cloud base. As seen in the left panel of Fig. 5, that expectation is not borne out in the ensemble. The correlation is no better when taken with respect to precipitation at the surface or its loss below cloud base. Furthermore, there is little correlation between the minimum buoyancy flux and any of these precipitation diagnostics.

As seen in Fig. 5, δq_t is strongly anti-correlated with LWP. Thus, well-mixed boundary layers are associated with thicker clouds here, as in non-precipitating simulations (Stevens et al. 2005b). This positive result leads us to follow the lead of that study and to investigate the relationships between LWP, entrainment, radiative cooling, and precipitation.

Entrainment heating and radiative cooling can be computed directly from the reported time series of z_i and radiative flux profiles, but we find that in doing so, variability in the inversion structure among different models obscures the relationships, as also found by Stevens et al. (2005b). Therefore we present analysis of mixed-layer budgets, which provide stronger trends. Heat and moisture budgets are given by

$$z_{i+} \frac{d\hat{\theta}_l}{dt} = E\Delta_+\theta_l + \frac{F_{\theta_l,0} + R_0 - \Delta F_{\text{rad}}}{\hat{\rho}c_p} \quad (8)$$

$$z_{i+} \frac{d\hat{q}_t}{dt} = E\Delta_+q_t + \frac{F_{q_t,0} - R_0}{\hat{\rho}L} \quad (9)$$

where E is the entrainment rate, $F_{\theta_l,0}$ and $F_{q_t,0}$ are surface fluxes excluding precipitation (R_0), $\Delta F_{\text{rad}} = F_{\text{rad}}(z_{i+}) - F_{\text{rad}}(0)$ is net emission of longwave radiation from the boundary layer, $\hat{\rho}$ is average air density in the boundary layer, and all fluxes are in energy units (e.g., W m^{-2}). Boundary-layer averages and jumps above the boundary layer are defined by

$$\hat{\psi} = \frac{1}{z_{i+}} \int_0^{z_{i+}} \psi dz \quad (10)$$

$$\Delta_+\psi = \psi(z_{i+}) - \hat{\psi} \quad (11)$$

in which z_{i+} is located 50 m above z_i . Here we generalize the non-dimensional entrainment

rate of Stevens et al. (2005b) to include precipitation:

$$\alpha = \frac{\hat{\rho}c_p E \Delta_+ \theta_l + R_0}{\Delta F_{\text{rad}}} \quad (12)$$

such that $\alpha = 1$ indicates a balance between the only heat sources and heat sink allowed to vary in these simulations, as $F_{\theta_l,0}$ is fixed. We evaluate α from model output by first solving for E from Eq. 9 and then for ΔF_{rad} from Eq. 8. Any relationships evident in Fig. 6 between LWP and the terms in α are noisy: E is generally flat for LWP $< \simeq 115 \text{ g m}^{-2}$ and declines beyond, and ΔF_{rad} generally rises up to roughly the same LWP and also then declines. Combining terms yields a strong anti-correlation between α and LWP. That is, when radiative cooling increases relative to warming by entrainment and precipitation, LWP tends to increase, with a Spearman rank correlation significant at the $2.4\text{-}\sigma$ level. (The most prominent outlier to the trend has somewhat diminished radiative cooling and an especially strong inversion, with $\Delta_+ \theta_l$ more than 2 K greater than in the other simulations.)

The general trend between LWP and α echoes Stevens et al. (2005b), but with the addition of precipitation here and in a different LWP regime: the smallest LWP in this ensemble is greater than any in that study. We caution that α is not intended to be a parameter that is universal to the study of mixed-layer dynamics, but is rather a convenient metric for comparing these simulations. For that matter, the placement of terms in α is not unique. Another possibility would be to subtract R_0 from the denominator instead of adding it to the numerator, yielding a dimensionless entrainment rate that correlates equally well with LWP here. It is seen in Table 2 that the ensemble median α (which happens to be the same as the mean value) is within a standard deviation of the mean derived from the measurements.

An obvious question to ask is, what drives the differences in α ? To simplify matters, in this system the possibilities can be reduced to dynamics and microphysics. The importance of dynamics can be assessed by comparing α from model simulations with and without microphysics (that is, including neither cloud-water sedimentation nor drizzle). As seen in Fig. 7, the strong correlation between α with and without microphysics suggests that

dynamics plays a dominant role in the spread of α .

As noted above, the previous BLCWG study found that models that limit subgrid-scale mixing at cloud top were better able to maintain thick cloud layers. The two models in that study with the smallest α values were UCLA and DHARMA, which is again the case here for the simulations without microphysics. A notable difference between the α ranking in the previous study and that here is that MetO was in the upper quartile previously, but is in the lower quartile here. The relative change between the two studies is likely attributable to the MetO model using a monotone advection scheme for momentum here, which dampens model energetics at cloud top and thereby reduces entrainment. As in the previous BLCWG intercomparison, when subgrid-scale mixing is increased in the COAMPS model – swapping a prognostic TKE scheme for a diagnostic mixing model – entrainment and α increase and LWP decreases, and the tendency holds with cloud-water sedimentation and drizzle included. Thus, although the air overlying the boundary layer in the present case is somewhat cooler and moister than in the previous study, the relationship between subgrid-scale mixing, entrainment, and LWP seems to be along the same lines as found previously.

While model dynamics evidently plays a leading role in determining the spread in α , microphysics cannot be dismissed. For instance, increasing the propensity to drizzle in the UCLA model increases α by $\sim 10\%$, largely attributable to a quintupling of R_0 . The increase of R_0 in the numerator of α is offset slightly by a decrease in entrainment heating. A less dramatic increase in the propensity to drizzle in DHARMA results in a milder response of R_0 , which is largely offset by increased entrainment, resulting in little change of α .

Considering that R_0 appears in the numerator, it may come as a surprise that including cloud-water sedimentation and drizzle together consistently diminishes α . Evidently the associated decrease in entrainment warming exceeds the net latent heating from precipitation in all cases here.

In the majority of simulations, LWP increases in response to including cloud-water sedi-

mentation and drizzle together. As seen in Fig. 8, the net change can be broken down into an increase in response to cloud-water sedimentation in all cases, and a decrease in response to drizzle in all but one case. The two models² showing appreciable net decrease in LWP correspond to the two models with the mildest LWP response to cloud-water sedimentation. As seen in Fig. 9, the only model in which LWP increases in response to drizzle also happens to be the model producing the smallest precipitation profile peak. This precipitation peak is smaller than those in any simulation with only cloud-water sedimentation (not shown), which may explain a response of LWP to drizzle in this case being in the same sense as a response to cloud-water sedimentation for all the models.

In an intercomparison of single-column models using the same specifications (Wyant et al. 2007), LWP also decreased in response to including drizzle in most cases. Additionally, LWP was found to increase in response to including cloud-water sedimentation, as found here.

d. Effects of Cloud-Water Sedimentation on Vertical Winds

Negative w skewness in stratocumulus has been reported elsewhere, in field measurements (e.g., Nicholls and Leighton 1986; Stevens et al. 2005b) as well as in model simulations (e.g., Bougeault 1985; Moeng 1986), a topic discussed in detail by Moeng and Rotunno (1990). Beyond the effects of cloud-water sedimentation already discussed here, we also find that cloud-water sedimentation affects $\overline{w^3}$ in the cloud layer, as seen in Fig. 3.

To isolate the impact of cloud-water sedimentation, we first consider non-drizzling DHARMA simulations in which cloud-water sedimentation is parameterized using Eq. 7. As seen in Fig. 10, vertical winds are negatively skewed throughout the cloud layer in the simulation without cloud-water sedimentation, but including it as prescribed (with $\sigma_g = 1.5$) not only reverses the sign of $\overline{w^3}$ but also reduces $\overline{w^2}$ throughout most of the cloud layer. Also, the vertical gradient of q_t increases with increasing cloud-water sedimentation (not shown), evidence of reduced mixing between the cloud and sub-cloud layers. The response of convection

²More accurately referred to as model configurations, since the sign of the LWP response in the UCLA model depends on the drizzle parameterization used.

in the cloud layer to intense cloud-water sedimentation thus resemble those of heavy drizzle found by Stevens et al. (1998). Evidence discussed further below suggests that the same mechanism plays a principal role here: drier downdrafts, resulting from a substantial sedimentation flux divergence at cloud top, lose their evaporatively-driven negative buoyancy above the mean cloud base, which leads to downdrafts weakening and updrafts dominating vertical mixing, resulting in more cumuliform convection.

Recalling that the cloud-droplet size distribution was specified as overly broad, we also consider a non-drizzling simulation using a narrower distribution, which nearly halves the sedimentation rate for a given cloud water and droplet number concentration. As seen in Fig.10 the effect of reduced cloud-water sedimentation on $\overline{w^3}$ in the cloud layer is still significant, with a profile that falls between that without and that with stronger cloud-water sedimentation. The reduced cloud-water sedimentation has far less impact on $\overline{w^2}$, which changes little relative to the results without cloud-water sedimentation. The average LWP and entrainment rates for the three DHARMA simulations (no sedimentation, and $\sigma_g = 1.2$ and 1.5) are respectively 127, 145, and 149 g m⁻² and 0.68, 0.59, and 0.51 cm s⁻¹. These results can be compared with a recent study (Bretherton et al. 2007) that considered the effects of cloud-water sedimentation (using the parameterization developed for this study), in non-drizzling simulations using SAM (a model included in the ensemble here) under different environmental conditions, the idealization of DYCOMS-II RF01 from the previous BLCWG intercomparison. As cloud-water sedimentation was sequentially turned on and then σ_g increased by Bretherton et al. (2007), the entrainment rate steadily decreased, LWP steadily increased, and $\overline{w^2}$ in the 50 m below the inversion held steady. As in that study, sequentially turning on and then increasing the strength of cloud-water sedimentation produces a steady trend of entrainment diminishing while $\overline{w^2}$ near cloud top does not change in the non-drizzling DHARMA simulations. But here the trend of increasing LWP largely stalls out as σ_g is increased. Furthermore, Bretherton et al. (2007) found cloud-water sedimentation to result in $\overline{w^2}$ increasing throughout much of the boundary layer, but here the effect on the

$\overline{w'^2}$ profile is just the opposite.

Using the environmental conditions of RF01, the response of non-drizzling DHARMA simulations to cloud-water sedimentation is consistent with those of Bretherton et al. (2007). The novel nonlinear response of $\overline{w'^2}$ to cloud-water sedimentation in the RF02 simulations here occurs in the presence of sedimentation that is much more intense than in the RF01 simulations. In DHARMA simulations without drizzle or cloud-water sedimentation, cooler and moister air overlying the boundary layer results in a peak cloud-water mixing ratio that is $\sim 50\%$ greater for RF02 than for RF01 conditions. Combined with a cloud-droplet number concentration in this RF02 case that is less than half that in the RF01 observations (vanZanten et al. 2005), the cloud-water sedimentation rate near cloud top is quadrupled compared to RF01. The strong cloud-water sedimentation flux divergence at cloud top evidently results in appreciably drier downdrafts, which become unsaturated above mean cloud base for the RF02 simulations. Thus, as seen in the right panels of Fig. 12, while the fraction of unsaturated air in the lower half of the cloud layer is unaffected by cloud-water sedimentation for the RF01 conditions, for the RF02 conditions more of the air above the mean cloud base becomes unsaturated in response to cloud-water sedimentation, particularly for $\sigma_g = 1.5$. This evidence thus suggests that the potential buoyancy mechanism of Stevens et al. (1998) can play an important role in cloud-layer dynamics whenever the sedimentation flux divergence at cloud top, whether from drizzle or cloud-water sedimentation, is strong enough to create gaps in the cloud layer.

In the RF02 simulations the gradient of q_l at cloud top is notably reduced as σ_g is increased from 1.2 to 1.5. This reduction affects both the radiative cooling profile and the moisture available for evaporation in the entrainment zone. Bretherton et al. (2007) found that the change in the radiative cooling profile associated with cloud-water sedimentation played a secondary role in reducing entrainment for the RF01 conditions, a conclusion we cannot test with the results here. However, the nearly linear response of entrainment to the sedimentation flux in RF02 suggests that the relative importance of these two processes is

not changing greatly as sedimentation strengthens.

Given the overly broad cloud-droplet size distribution assumed in the specifications and the nearly 20% increase of entrainment in these non-drizzling simulations when the narrower distribution is used, it is likely that entrainment rates in drizzling simulations with parameterized cloud-water sedimentation would have been greater had a more appropriate value of $\sigma_g = 1.2$ been specified. Thus, the middle half of the ensemble likely would have matched the measurements better (Fig. 1 and Table 2).

Finally, we consider the impacts of cloud-water sedimentation on vertical winds across the ensemble. As seen in the upper panels of Fig. 11, including cloud-water sedimentation increases $\overline{w'^3}$ near cloud base for all but one model. For simulations without drizzle, allowing cloud water to sediment results in $\overline{w'^3}$ near cloud base changing sign, from negative to positive, for all but two models. Including drizzle reduces the impact of cloud-water sedimentation on cloud-base $\overline{w'^3}$ for nearly all the models, but continues to reverse its sign in most cases. Regarding convective intensity near cloud top (lower panels of Fig. 11), $\overline{w'^2}$ decreases in the 50 m below z_i in about half of the simulations without drizzle, while it decreases in nearly all cases when averaged over twice that depth. In simulations with drizzle included, cloud-water sedimentation leads to $\overline{w'^2}$ near cloud top decreasing in nearly all the simulations, averaged over either depth. Including cloud-water sedimentation also results in other statistics indicative of a more cumuliform regime: the relative dispersion (standard deviation divided by the mean) of cloud-base height, inversion height, and LWP increase in all simulations, except for RAMS without drizzle (not shown).

4. Discussion

In the previous BLCWG intercomparison (Stevens et al. 2005b), it was found that the entrainment rates in nearly all the baseline simulations were substantially greater than the measured estimate of 0.38 cm s^{-1} (Stevens et al. 2003b), and excessive entrainment resulted in simulated LWP values far less than that implied by the measurements: cloud thickness and

maximum q_l in the supplemental material of Stevens et al. (2003a) indicate LWP $\simeq 90 \text{ g m}^{-2}$, $\sim 50\%$ greater than the maximum in the simulations. That study concluded that progress was needed to limit entrainment through reduced subgrid-scale mixing at cloud top. However, cloud-water sedimentation was not considered in the previous intercomparison. And while the models that parameterize the process here exaggerate its intensity because an overly broad cloud-droplet size distribution was used, there is no reason to doubt that cloud droplets fall relative to the air, and that their falling reduces entrainment and, at least under relatively dry inversions, leads to LWP increasing. Non-drizzling RF01 simulations, both here and in Bretherton et al. (2007), indicate that a portion of the systematic overprediction of entrainment and underprediction of LWP in at least two of the models in the previous intercomparison resulted from omitting this simple physical process. Which is not to claim that the systematic errors in the treatment of subgrid-scale mixing at cloud top, as discussed by Stevens et al. (2005b), do not generally play an even greater role in the overprediction of entrainment. As a caveat, we cannot rule out the possibility that an inability to resolve entrainment processes at cloud top produces artifacts in the response of entrainment to a sedimentation flux divergence at cloud top, whether from cloud droplets or drizzle. It seems nonetheless clear that cloud-water sedimentation should not be omitted from simulations of stratocumulus, as has been long done by models that parameterize cloud microphysics. Also, it is quite likely that this process is important to other cloud types, and presumably the lesson carries over to the treatment of cloud ice in mixed-phase and cold clouds. Unfortunately the treatment of cloud-water sedimentation introduces further parameters to the microphysical mix. By assuming a simple analytic form for the cloud-droplet size distribution, here we limit the additional requirements to a single parameter.

The suitability of the observed system for evaluating model fidelity is worth pondering here. One of our goals was to evaluate which microphysical schemes might best reproduce the observed drizzle profile. Yet the choice of a case study was less than ideal, if for no other reason than the considerable heterogeneity of the observed cloud field, a bimodal

population of open and closed cells, the former drizzling heavily and the latter far less so. In retrospect, an idealization of their average is a problematic target for models. As noted earlier, given the non-linearity of the drizzle process with respect to N_d and LWP, results of such a comparison are likely to be unfavorable even if the models and measurements are perfect. A more homogeneous cloud field would be a better target. With regard to drizzling stratocumulus, the seventh research flight of DYCOMS-II would seem to be a good candidate.

Beyond such difficulties intrinsic to this case study, one can further ask if the fidelity of the representation of any single process can truly be isolated in our approach. For instance, given measurements of a more homogeneous cloud field, would there be a better prospect of determining which microphysics schemes best represent drizzle? Considering that differences in simulations result from a complex mix of all the model subcomponents, it is difficult to be optimistic in this regard. It might have been expected that, by virtue of a common approach, the two models with bin microphysics (DHARMA and RAMS) would have distinguished themselves from the rest. But a number of diagnostics indicate just the opposite, as any commonality in microphysical approach between these two models is clearly swamped by differences in dynamics (e.g., without microphysics these two had respectively the lowest and highest values of α in the ensemble). A more fruitful approach could be to swap a model subcomponent of interest (such as microphysics) among an assortment of models to see if any tended to produce results more faithful to some sample of case studies that are well constrained and lacking obvious deficiencies.

5. Summary

We have compared large-eddy simulations based on an idealization of the second research flight of the DYCOMS-II field project, which sampled a bimodal population of heavily drizzling pockets of open cellular convection amid lightly drizzling, overcast stratocumulus. Results of six-hour, nocturnal simulations from eleven groups were used. Two models used bin

microphysics schemes, which resolve the size distributions of aerosol and cloud particles and explicitly treat cloud microphysical processes. The remaining models fixed the cloud-droplet concentration and parameterized drizzle microphysics by a variety of schemes. A simple parameterization of cloud-water sedimentation was devised for those models, and simulations were run with and without drizzle, each with and without cloud-water sedimentation. Additionally, two of the groups considered variations in the efficiency of drizzle production. Most of the analysis focused on the final four hours of simulations that included cloud-water sedimentation and drizzle. Our principal findings follow.

- The mean liquid water path (LWP) of the simulation ensemble reproduces the observed mean LWP observation remarkably well, but the mean entrainment rate is at the lower end of the observations, and the ensemble-average maximum vertical wind variance is roughly half that measured.

- The mean third moment of the vertical wind was observed to be negative near cloud base, indicating downdrafts stronger than updrafts; in contrast $\overline{w'^3}$ was positive near cloud base in the simulations. Cloud-water sedimentation leads to increased $\overline{w'^3}$ near cloud base for all the simulations with drizzle, and cloud-water sedimentation reverses the sign of $\overline{w'^3}$ near cloud base for all but two of the simulations without drizzle.

- Decoupling of the cloud and sub-cloud layers, as measured by the vertical gradient of total moisture, increases as the maximum variance of the vertical wind decreases, though neither correlate well with precipitation, either at cloud base, at the surface, or in terms of its fractional loss below cloud base.

- LWP increases with the ratio of radiative cooling to the sum of latent heating associated with precipitation plus entrainment warming, and this response is largely determined by dynamics, though LWP does decrease as the propensity for drizzle is increased.

- Sedimentation of cloud water consistently results in decreased entrainment and increased LWP, as found elsewhere. In contrast to results from a study with a far smaller sedimentation flux, convective intensity (in terms of $\overline{w'^2}$) tends to decrease in response to

cloud-water sedimentation here.

- Including drizzle consistently leads to a reduction in entrainment, leading to a decrease in LWP for all but one of the models.

Thus we find that the effects on LWP of cloud-water sedimentation and drizzle oppose each other, and on average cloud-water sedimentation dominates here. Drizzle is not all that strong in the simulations, which serves to favor the dominance of the LWP impact of cloud-water sedimentation. Considering the net effect of cloud-water sedimentation and drizzle, a drier or warmer inversion would likely favor the impact of cloud-water sedimentation, and a moister or cooler one would favor the impact of drizzle. Regardless, we strongly recommend against ignoring sedimentation of cloud water, as has long been done.

6. Acknowledgments

The first author was supported by NASA’s Radiation Sciences program. Krueger and Zulauf were supported by the NSF through Grant ATM-0346854. We thank Ann Fridlind for helpful discussions, and Robert Wood for raising thought-provoking questions.

7. Appendix A: Aerosol Size Distributions

The bin microphysics models (DHARMA and RAMS) treat aerosols diagnostically (see Stevens et al. 1996). There was considerable variability in the aerosol size distributions measured during RF02, not only between the regions of open and closed cells, but also between the boundary layer and the overlying air. We ignore that complexity and specify a uniform aerosol distribution, obtained by subjectively matching the aerosol size distribution obtained during 30 minutes of flight below cloud base (Fig. 13) with two log-normal size distributions assumed to consist of ammonium bisulfate (with molecular weight 115 g/mol, dry density 1.78 g cm^{-3} , and two ions dissolved per molecule). The total number, mode radius, and geometric standard deviation for the two modes are 125 and 65 cm^{-3} , 0.011 and $0.06 \text{ }\mu\text{m}$,

and 1.2 and 1.7, respectively. The coincident measurements of cloud condensation nuclei (CCN) performed by the University of Wyoming (Snider et al. 2006) are seen in the right panel to agree with the cumulative CCN distribution based on the measured size distribution and assumed chemical composition of the aerosol. For the sake of reducing differences between models, aerosol numbers were repartitioned between the two modes through trial and error, such that the average cloud droplet number concentration in cloudy grid cells roughly matches the fixed value of 55 cm^{-3} used by models without bin microphysics. This adjustment was not substantial for DHARMA, with total aerosol numbers set to 115 and 75 cm^{-3} in the small and large modes, respectively.

8. Appendix B: Model Descriptions

Nearly all the models solve equations for u , v , w , θ_l , and q_t (or specific humidity in some models) in three dimensions; the COAMPS, JAMSTEC, MetO, and University of Reading models carry different temperature or moisture variables, as described below. Additional microphysical variables for computing drizzle vary among the models, and are described below. All the models treat state variables as uniform within a grid cell, except for WVU, which treats fractional cloudiness within grid cells. All except NHM, RAMS, and the University of Utah models invert Poisson equations to maintain continuity, uniformly based on fast Fourier transforms in the horizontal and an inversion of a tridiagonal matrix (in Fourier space) in the vertical.

The three-dimensional mesh was specified intercomparison to be 128×128 in the horizontal with uniform spacing of 50 m and cyclic boundary conditions. The vertical grid (Fig. 14) was specified as 96 layers with layer thickness $\Delta z = 5 \text{ m}$ near the surface, a \sin^2 stretching within the boundary layer (with a maximum $\Delta z = 25.2 \text{ m}$ at $z = 400 \text{ m}$), and a 125-m deep region with $\Delta z = 5 \text{ m}$ starting at $z = 795 \text{ m}$, with Δz stretching above to a maximum of 81.4 m at $z = 1500 \text{ m}$, the top of the domain. All of the models used the specified grid, except for MPI, which used a uniform $\Delta z = 5 \text{ m}$, and RAMS, which used Δz

= 10 m up to $z = 950$ m and stretching above. (A preliminary grid, which did not include the uniform region of 5-m spacing above the inversion, resulted in a positive feedback in which entrainment increased with grid spacing above the initial inversion.) It was recommended to translate model domains at a velocity corresponding to the boundary-layer mean wind of $(u, v) = (5, -5.5)$ m s⁻¹ to minimize numerical errors associated with advection. A sponge layer was recommended to dampen any trapped buoyancy waves above the inversion, with a nudging coefficient increasing with \sin^2 vertical dependence from zero at $z = 1250$ m to $(100 \text{ s})^{-1}$ at the top of the domain. Brief descriptions of the model configurations used in the intercomparison follow.

COAMPS^{®3}. Solutions provided by J.-C. Golaz. LES version of COAMPS described in Golaz et al. (2005). With the exception of pressure solver, model dynamics are unchanged from Stevens et al. (2005b); compressible equations have been replaced with anelastic equations. In the default configuration, a prognostic subgrid-scale (SGS) mixing model was used (Deardorff 1980b); results also submitted using a Smagorinsky-Lilly diagnostic treatment, denoted COAMPS_SL. The microphysics model, based on Khairoutdinov and Kogan (2000, hereafter KK), carries potential temperature (θ), q_v , cloud water mixing ratio (q_c), q_r , and number concentration of drizzle drops (N_r) as prognostic variables.

DHARMA: Solutions provided by A. Ackerman. Model dynamics unchanged from DHARMA-0 in Stevens et al. (2005b). A single-moment bin microphysics scheme is used (see Ackerman et al. 2004, and references therein) resolving size distributions of aerosols and activated water drops each into 20 size bins, spanning particle radii of 0.01–2.6 and 1–260 μm , respectively. Mass concentration of solute within each drop size bin is carried, doubling the number of microphysical prognostic variables. Drop collision efficiencies follow Hall (1980). Coalescence efficiencies (E_{coal}), which follow Beard and Ochs (1984), are extrapolated beyond the measurement range of Beard and Ochs (1984) and limited between 0.5 and unity. An alternative is also considered, denoted DHARMA_BO, in which $E_{\text{coal}} = 1$ beyond size range of Beard

³COAMPS is a registered trademark of the Naval Research Laboratory

and Ochs (1984).

MetO. UK Met Office (MetO) solutions provided by A. Lock. Model dynamics unchanged from Stevens et al. (2005b), except here monotone advection used for all fields, including momentum. Microphysics model carries q_v , q_c , q_r , and N_r as prognostic variables. Auto-conversion of q_c to q_r follows KK. Fall speed of drizzle drops is an approximate fit to Beard (1976) over a drop radius range of 40–70 μm .

MPI. Max Planck Institute (MPI) solutions provided by A. Chlond. Model dynamics unchanged from MPI-0 in Stevens et al. (2005b), except here the coordinate system is translated with mean geostrophic wind. Microphysics model follows the Lüpkes (1991) three-variable scheme, partitioning condensate into cloud water and rainwater. N_r is prognostic, and cloud water content is diagnosed at each time step as the residual between total water content and the saturation vapor content plus the prognosed rainwater.

NHM. Non-Hydrostatic Model (NHM) solutions provided by K. Nakamura. The model, developed by the Meteorological Research Institute at the Japan Meteorological Agency, solves fully compressible equations, treating advection with a monotonic centered difference scheme and time stepping with a leapfrog method using an Asselin time filter. Subgrid-scale model is based on Klemp and Wilhelmson (1978) and Deardorff (1980b). Microphysics model carries θ , q_v , q_c , and q_r as prognostic variables. The least aggressive autoconversion scheme used by Richard and Chaumerliac (1989), referred to therein as BR2, is used here. Accretion of cloud droplets by rain drops, condensation, and sedimentation of rain drops are based on Lin et al. (1983); further details provided by Saito et al. (2001).

Reading. University of Reading solutions provided by S. Weinbrecht, using the MetO model described above, but with a different SGS model, a revised version of the stochastic backscatter model of Weinbrecht and Mason (2008). SGS model is based on Mason and Thomson (1992) but the implementation was improved to ensure an appropriate scale of backscatter, independent of mesh refinement, and is isotropic.

RAMS. Regional Atmospheric Modeling System (RAMS) solutions provided by H. Jiang.

Model dynamics unchanged from Stevens et al. (2005b). A double-moment bin microphysics scheme is used for microphysics, predicting both drop number and mass in each of 33 size bins, with mass doubling between bins, spanning drop radii of $1.56 \mu\text{m} - 2.54 \text{mm}$. Microphysics scheme is described by Tzivion et al. (1987), Tzivion et al. (1989) and Stevens et al. (1996). Gravitational collision efficiencies follow Hall (1980), and $E_{\text{coal}} = 1$. Solute and curvature effects are ignored in the treatment of condensation and evaporation.

SAM. System for Atmospheric Modeling (SAM) solutions provided by M. Khairoutdinov. Model dynamics unchanged from Stevens et al. (2005b), and microphysics parameterization described by KK.

UCLA. University of California, Los Angeles (UCLA) solutions provided by V. Savic-Jovicic and B. Stevens. Model dynamics unchanged from UCLA-0 in Stevens et al. (2005b), although here SGS diffusivity is damped with distance from the surface, with a 100-m length scale, to more smoothly match boundary conditions. Away from the surface SGS scalar fluxes were carried by numerical dissipation of advection scheme. The microphysics scheme carries q_r and N_r as prognostic variables; q_c is diagnosed as the positive definite residual between equilibrium q_l and prognosed q_r . Microphysics follows two prescriptions, one KK and the other Seifert and Beheng (2001, 2006); denoted respectively as UCLA and UCLA_SB. In both implementations, cloud droplets correspond to radii less than $25 \mu\text{m}$.

Utah. University of Utah solutions provided by M. Zulauf and S. Krueger. The model (Zulauf 2001) solves compressible equations using the quasi-compressibility approximation of Droegemeier and Wilhelmson (1987). Scalar advection uses third-order upwinding (Stevens and Bretherton 1996), with monotonicity maintained using flux-corrected transport (Zalesak 1979). Momentum advection uses the third-order upwinding scheme of Wicker and Skamarock (1998), which also provides the basis for the time-split second-order Runge-Kutta time stepping. SGS mixing is parameterized with a prognostic TKE scheme (Deardorff 1980b). Microphysics uses a saturation adjustment step, along with a single-moment, mixed-phase bulk scheme (Lin et al. 1983; Lord et al. 1984; Krueger et al. 1995b). Autocon-

version follows modified Liu and Daum (2004) formula in Wood (2005b), using the threshold function from Liu et al. (2005).

WVU. West Virginia University (WVU) solutions provided by D. Lewellen. Model dynamics unchanged from WVU-0 in Stevens et al. (2005b). A bulk Kessler-type microphysics scheme is used, carrying q_r and N_r as prognostic variables. Parameterizations for autoconversion, accretion, evaporation, and fall speeds follow KK.

9. Appendix C: Description of Model Output Files

The netCDF output files archived at the GCSS DIME website consists of all the requested time series and profiles, as described in Tables 3 and 4.

REFERENCES

- Ackerman, A. S., M. P. Kirkpatrick, D. E. Stevens, and O. B. Toon, 2004: The impact of humidity above stratiform clouds on indirect aerosol climate forcing. *Nature*, **432**, 1014–1017.
- Ackerman, A. S., O. B. Toon, and P. V. Hobbs, 1993: Dissipation of marine stratiform clouds and collapse of the marine boundary layer due to the depletion of cloud condensation nuclei by clouds. *Science*, **262**, 226–229.
- Ackerman, A. S., O. B. Toon, J. P. Taylor, D. W. Johnson, P. V. Hobbs, and R. J. Ferek, 2000: Effects of aerosols on cloud albedo: Evaluation of Twomey’s parameterization of cloud susceptibility using measurements of ship tracks. *J. Atmos. Sci.*, **57**, 2684–2695.
- Albrecht, B., 1989: Aerosols, cloud microphysics, and fractional cloudiness. *Science*, **245**, 1227–1230.

- Beard, K. V., 1976: Terminal velocity and shape of cloud and precipitation drops aloft. *J. Atmos. Sci.*, **33**, 851–864.
- Beard, K. V. and H. T. Ochs, 1984: Collection and coalescence efficiencies for accretion. *J. Geophys. Res.*, **89(D5)**, 7165–7169.
- Bony, S. and J. Dufresne, 2005: Marine boundary layer clouds at the heart of tropical cloud feedback uncertainties in climate models. *Geophys. Res. Lett.*, **32 (L20806)**.
- Bougeault, P., 1985: The diurnal cycle of the marine stratocumulus layer: A higher-order model study. *J. Atmos. Sci.*, **42 (24)**, 2826–2843.
- Bretherton, C., P. Blossey, and J. Uchida, 2007: Cloud droplet sedimentation, entrainment efficiency, and subtropical stratocumulus albedo. *Geophys. Res. Lett.*, **34 (L03813)**.
- Bretherton, C. and M. Wyant, 1997: Moisture transport, lower-tropospheric stability, and decoupling of cloud-topped boundary layers. *J. Atmos. Sci.*, **54**, 148–167.
- Brost, R., J. Wyngaard, and D. Lenschow, 1982: Marine stratocumulus layers. Part II: Turbulence budgets. *J. Atmos. Sci.*, **39 (4)**, 818–836.
- Coakley, J. A., Jr. and C. D. Walsh, 2002: Limits to the aerosol indirect radiative effect derived from observations of ship tracks. *J. Atmos. Sci.*, **59**, 668–680.
- Comstock, K. K., R. Wood, S. E. Yuter, and C. S. Bretherton, 2004: Reflectivity and rain rate in and below drizzling stratocumulus. *Quart. J. Roy. Meteor. Soc.*, **130**, 2891–2918.
- Deardorff, J. W., 1980a: Cloud top entrainment instability. *J. Atmos. Sci.*, **37**, 131–147.
- Deardorff, J. W., 1980b: Stratocumulus-capped mixed layers derived from a three-dimensional model. *Bound.-Layer Meteor.*, **18**, 495–527.

- Droegemeier, K. K. and R. B. Wilhelmson, 1987: Numerical simulation of thunderstorm outflow dynamics. Part I: Outflow sensitivity experiments and turbulence dynamics. *J. Atmos. Sci.*, **44**, 1180–1210.
- Faloona, I., et al., 2005: Observations of entrainment in eastern Pacific marine stratocumulus using three conserved scalars. *J. Atmos. Sci.*, **62**, 3268–3285.
- Golaz, J.-C., S. Wang, J. D. Doyle, and J. M. Schmidt, 2005: COAMPS[®]-LES: Model evaluation and analysis of second and third moment vertical velocity budgets. *Bound.-Layer Meteor.*, **116**, 487–517.
- Hall, W. D., 1980: A detailed microphysical model within a two-dimensional dynamic framework: Model description and preliminary results. *J. Atmos. Sci.*, **37**, 2486–2507.
- Khairoutdinov, M. F. and Y. L. Kogan, 2000: A new cloud physics parameterization in a large-eddy simulation model of marine stratocumulus. *Mon. Wea. Rev.*, **128**, 229–243.
- Klein, S. and D. Hartmann, 1993: The seasonal cycle of low stratiform clouds. *Journal of Climate*, **6** (8), 1587–1606.
- Klemp, J. B. and R. B. Wilhelmson, 1978: The simulation of three-dimensional convective storm dynamics. *J. Atmos. Sci.*, **35**, 1070–1096.
- Krueger, S., G. McLean, and Q. Fu, 1995a: Numerical simulation of the stratus-to-cumulus transition in the subtropical marine boundary layer. Part I: Boundary-layer structure. *J. Atmos. Sci.*, **52** (16), 2839–2850.
- Krueger, S. K., Q. Fu, K. N. Liou, and H.-N. S. Chin, 1995b: Improvements of an ice-phase microphysics parameterization for use in numerical simulations of tropical convection. *J. Appl. Meteor.*, **34**, 281–287.
- Larson, V. E., K. E. Kotenberg, and N. B. Wood, 2007: An analytic longwave radiation formula for liquid layer clouds. *Mon. Wea. Rev.*, **135**, 689–699.

- Lewellen, D. and W. Lewellen, 2002: Entrainment and decoupling relations for cloudy boundary layers. *J. Atmos. Sci.*, **59** (20), 2966–2986.
- Lin, Y.-L., R. D. Farley, and H. D. Orville, 1983: Bulk parameterization of the snow field in a cloud model. *J. Clim. Appl. Meteor.*, **22**, 1065–1092.
- Liu, Y. and P. H. Daum, 2004: Parameterization of the autoconversion process. Part I: Analytical formulation of the Kessler-type parameterizations. *J. Atmos. Sci.*, **61**, 1539–1548.
- Liu, Y., P. H. Daum, and R. L. McGraw, 2005: Size truncation effect, threshold behavior, and a new type of autoconversion parameterization. *Geophys. Res. Lett.*, **32**.
- Lord, S. J., H. E. Willoughby, and J. M. Piotrowicz, 1984: Role of a parameterized ice-phase microphysics in an axisymmetric, non-hydrostatic tropical cyclone model. *J. Atmos. Sci.*, **41**, 2836–2848.
- Lüpkes, C., 1991: *Untersuchungen zur Parametrisierung von Koagulationsprozessen niederschlagsbildender Tropfen*. Verlag Dr. Kovač, Hamburg, Germany.
- Martin, G. M., D. W. Johnson, and A. J. Spice, 1994: The measurement and parameterization of effective radius of droplets in warm stratocumulus clouds. *J. Atmos. Sci.*, **51**, 1823–1842.
- Mason, P. J. and D. J. Thomson, 1992: Stochastic backscatter in large-eddy simulations of boundary layers. *J. Fluid Mech.*, **242**, 51–78.
- Moeng, C., 1986: Large-eddy simulation of a stratus-topped boundary layer. Part I: Structure and budgets. *J. Atmos. Sci.*, **43**, 2886–2900.
- Moeng, C. and R. Rotunno, 1990: Vertical-velocity skewness in the buoyancy-driven boundary layer. *J. Atmos. Sci.*, **47**, 1149–1162.

- Nicholls, S., 1984: The dynamics of stratocumulus: Aircraft observations and comparisons with a mixed layer model. *Quart. J. Roy. Meteor. Soc.*, **110**, 783–820.
- Nicholls, S. and J. Leighton, 1986: An observational study of the structure of stratiform cloud sheets: Part I. Structure. *Quart. J. Roy. Meteor. Soc.*, **112** (472), 431–460.
- Paluch, I. and D. Lenschow, 1991: Stratiform cloud formation in the marine boundary layer. *J. Atmos. Sci.*, **48** (19), 2141–2158.
- Pawlowska, H. and J.-L. Brenguier, 2003: An observational study of drizzle formation in stratocumulus clouds for general circulation model (GCM) parameterizations. *J. Geophys. Res.*, **108**(D15), 8630.
- Petters, M. D., J. R. Snider, B. Stevens, G. Vali, I. Faloon, and L. Russell, 2006: Accumulation mode aerosol, pockets of open cells, and particle nucleation in the remote subtropical Pacific marine boundary layer. *J. Geophys. Res.*, **111**(D2), D02 206.
- Pincus, R. and M. B. Baker, 1994: Effect of precipitation on the albedo susceptibility of clouds in the marine boundary layer. *Nature*, **372**, 250–242.
- Platnick, S., et al., 2000: The role of background cloud microphysics in the radiative formation of ship tracks. *J. Atmos. Sci.*, **57**, 2607–2624.
- Randall, D., et al., 2003: Confronting models with data: The GEWEX Cloud Systems Study. *Bull. Amer. Meteor. Soc.*, **84**, 455–469.
- Randall, D. A., 1980: Conditional instability of the first kind upside-down. *J. Atmos. Sci.*, **37**, 125–130.
- Richard, E. and N. Chaumerliac, 1989: Effects of different rain parameterizations on the simulation of mesoscale orographic precipitation. *J. Appl. Meteor.*, **28**, 1197–1212.
- Rogers, R. R., 1979: *A Short Course in Cloud Physics*. 2d ed., Pergamon Press.

- Saito, K., T. Kato, H. Eito, and C. Muroi, 2001: Documentation of the Meteorological Research Institute/Numerical Prediction Division unified nonhydrostatic model. Tech. Rep. 16, Meteorological Research Institute–Japanese Meteorological Agency.
- Seifert, A. and K. D. Beheng, 2001: A double-moment parameterization for simulating autoconversion, accretion and self collection. *Atmos. Res.*, **59-60**, 265–281.
- Seifert, A. and K. D. Beheng, 2006: A two-moment cloud microphysics parameterization for mixed-phase clouds. Part 1: Model description autoconversion, accretion and self collection. *Meteorol. Atmos. Phys.*, **92**, 45–66.
- Snider, J. R., M. D. Petters, P. Wechsler, and P. Liu, 2006: Supersaturation in the Wyoming CCN instrument. *J. Atmos. Oceanic Technol.*, **23**, 1323–1339.
- Stevens, B., 2000: Cloud transitions and decoupling in shear-free stratocumulus-topped boundary layers. *Geophys. Res. Lett.*, **27 (16)**, 2557–2560.
- Stevens, B., W. R. Cotton, G. Feingold, and C.-H. Moeng, 1998: Large-eddy simulations of strongly precipitating, shallow, stratocumulus-topped boundary layers. *J. Atmos. Sci.*, **55**, 3616–3638.
- Stevens, B., G. Feingold, W. R. Cotton, and R. L. Walkso, 1996: Elements of the microphysical structure of numerically simulated nonprecipitating stratocumulus. *J. Atmos. Sci.*, **53**, 980–1006.
- Stevens, B., G. Vali, K. Comstock, M. C. vanZanten, P. H. Austin, C. S. Bretherton, and D. Lenschow, 2005a: Pockets of open cells (POCs) and drizzle in marine stratocumulus. *Bull. Amer. Meteor. Soc.*, **86**, 51–57.
- Stevens, B., et al., 2003a: Dynamics and chemistry of marine stratocumulus – DYCOMS-II. *Bull. Amer. Meteor. Soc.*, **84**, 579–593.

- Stevens, B. et al., 2003b: On entrainment rates in nocturnal marine stratocumulus. *Quart. J. Roy. Meteor. Soc.*, **129**, 3469–3493.
- Stevens, B. et al., 2005b: Evaluation of large-eddy simulations via observations of nocturnal marine stratocumulus. *Mon. Wea. Rev.*, **133**, 1443–1462.
- Stevens, D. E. and C. S. Bretherton, 1996: A new forward-in-time advection scheme and adaptive multilevel flow solver for nearly incompressible atmospheric flow. *J. Comput. Phys.*, **129**, 284–295.
- Turton, J. D. and S. Nicholls, 1987: Diurnal variation of stratocumulus. *Quart. J. Roy. Meteor. Soc.*, **113**, 969–1009.
- Twomey, S., 1974: Pollution and the planetary albedo. *Atmos. Environ.*, **8**, 1251–1256.
- Tzivion, S., G. Feingold, and Z. Levin, 1987: An efficient numerical solution to the stochastic collection equation. *J. Atmos. Sci.*, **44**, 3139–3149.
- Tzivion, S., G. Feingold, and Z. Levin, 1989: The evolution of raindrop spectra. Part II: Collisional collection/breakup and evaporation in a rain shaft. *J. Atmos. Sci.*, **46**, 3312–3327.
- Weinbrecht, S. and P. Mason, 2008: Stochastic backscatter for cloud-resolving models. Part I: Implementation and testing in a dry convective boundary layer. *J. Atmos. Sci.*, **65** (1), 123–139.
- Wicker, L. J. and W. C. Skamarock, 1998: A time-splitting scheme for the elastic equations incorporating second-order Runge-Kutta time differencing. *Mon. Wea. Rev.*, **126**, 1992–1999.
- Wood, R., 2005a: Drizzle in stratiform boundary layer clouds. Part I: Vertical and horizontal structure. *J. Atmos. Sci.*, **62**, 3011–3033.

- Wood, R., 2005b: Drizzle in stratiform boundary layer clouds. Part II: Microphysical aspects. *J. Atmos. Sci.*, **62**, 3034–3050.
- Wyant, M., et al., 2007: A single-column model intercomparison of a heavily drizzling stratocumulus-topped boundary layer. *J. Geophys. Res.*, **112**, D24 204.
- Zalesak, S. T., 1979: Fully multidimensional flux-corrected transport. *J. Comput. Phys.*, **31**, 335–362.
- vanZanten, M. C. and B. Stevens, 2005: Observations of the structure of heavily precipitating marine stratocumulus. *J. Atmos. Sci.*, **62**, 4327–4342.
- vanZanten, M. C., B. Stevens, G. Vali, and D. Lenschow, 2005: Observations of drizzle in nocturnal marine stratocumulus. *J. Atmos. Sci.*, **62**, 88–106.
- Zulauf, M. A., 2001: Modeling the effects of boundary layer circulations generated by cumulus convection and leads on large-scale surface fluxes. Ph.D. thesis, University of Utah, http://www.met.utah.edu/skrueger/publications/zulauf_dissert_2001.pdf, 177 pp., Salt Lake City, UT 84112.

List of Figures

1	Evolution of time series	38
2	Precipitation and cloud cover versus LWP	39
3	Ensemble profiles	40
4	Moisture gradient and minimum buoyancy flux versus maximum $\overline{w'^2}$	41
5	Moisture gradient versus cloud-base precipitation and LWP	42
6	Terms in mixed-layer analysis versus LWP	43
7	Effects of microphysics on model diagnostics	44
8	LWP and entrainment changes associated with microphysics	45
9	Peak precipitation versus drizzle-induced change in LWP	46
10	Vertical wind statistics for DHARMA simulations	47
11	Changes in dynamics associated with cloud-water sedimentation	48
12	Cloud-water sedimentation induced changes for RF01 and RF02 conditions	49
13	Measured aerosol size distributions	50
14	Vertical grid recommended for all models.	51

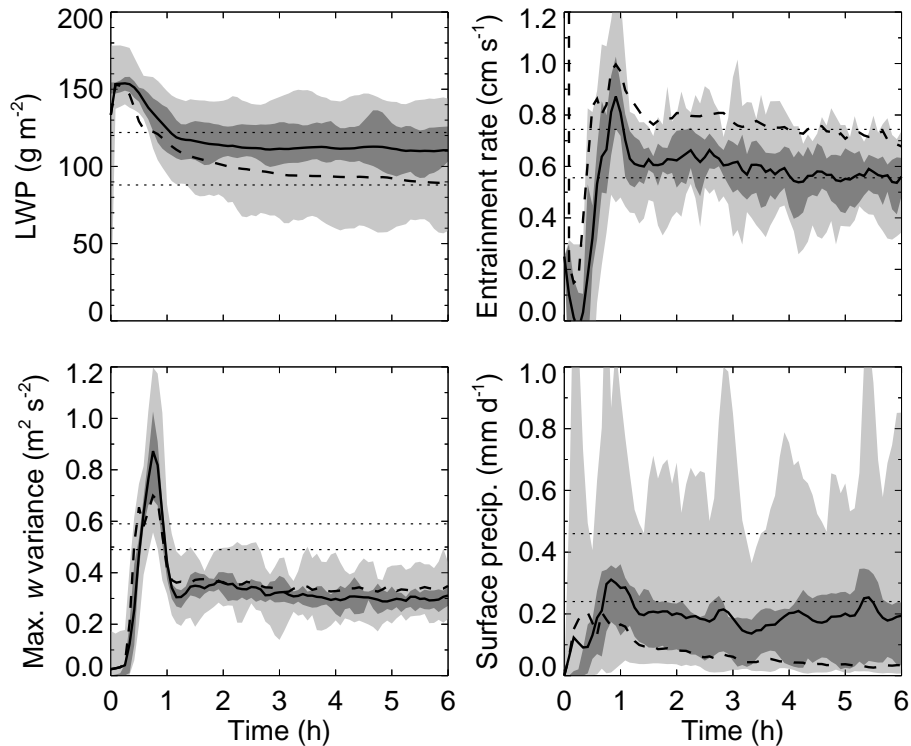


FIG. 1. Evolution of domain average LWP, entrainment rate (defined in text), maximum $\overline{w'^2}$ (peak value in the w'^2 profile), and surface precipitation for simulations that include cloud-water sedimentation and drizzle. Ensemble range, middle two quartiles, and mean denoted by light and dark shading, and solid lines, respectively. Ensemble mean from simulations that include drizzle but not cloud-water sedimentation denoted by dashed lines. Approximate ranges of measurement averages denoted by dotted lines, with upper and lower LWP values estimated from Stevens et al. (2003a) and aircraft soundings, respectively; entrainment rates from Faloon et al. (2005); maximum $\overline{w'^2}$ from vanZanten and Stevens (2005); and precipitation from vanZanten et al. (2005).

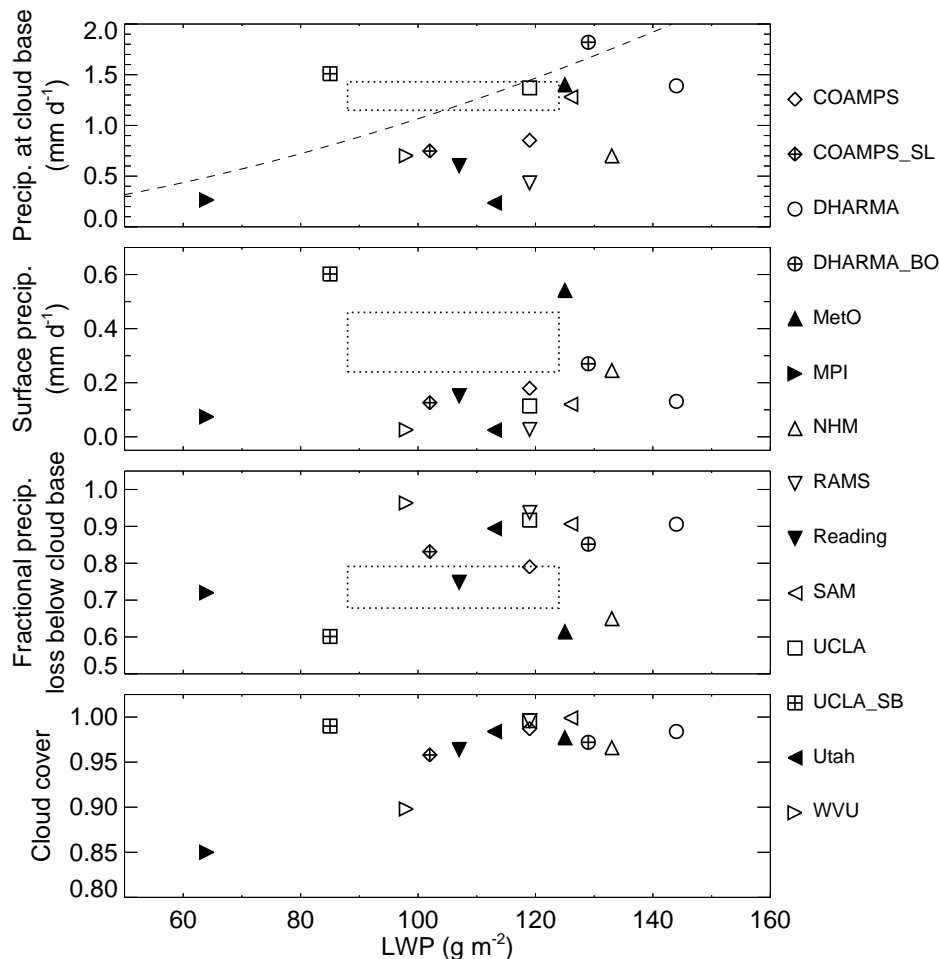


FIG. 2. Precipitation at cloud base, at the surface, their relative difference, and domain average cloud cover versus LWP, all averaged over last four hours of simulations that include cloud-water sedimentation and drizzle. Cloud base and cloud cover defined in Appendix C. Dotted boxes denote measurements (see Fig. 1). Symbol legend given at right. Dashed line is Comstock et al. (2004) fit to measurements of Peruvian stratocumulus, in which cloud base precipitation was found to scale with $(LWP/N_d)^{7/4}$, which we adapt by fixing $N_d = 55 \text{ cm}^{-3}$; other scaling relationships have been reported (e.g., Pawlowska and Brenguier 2003; vanZanten et al. 2005), as discussed by Wood (2005a).

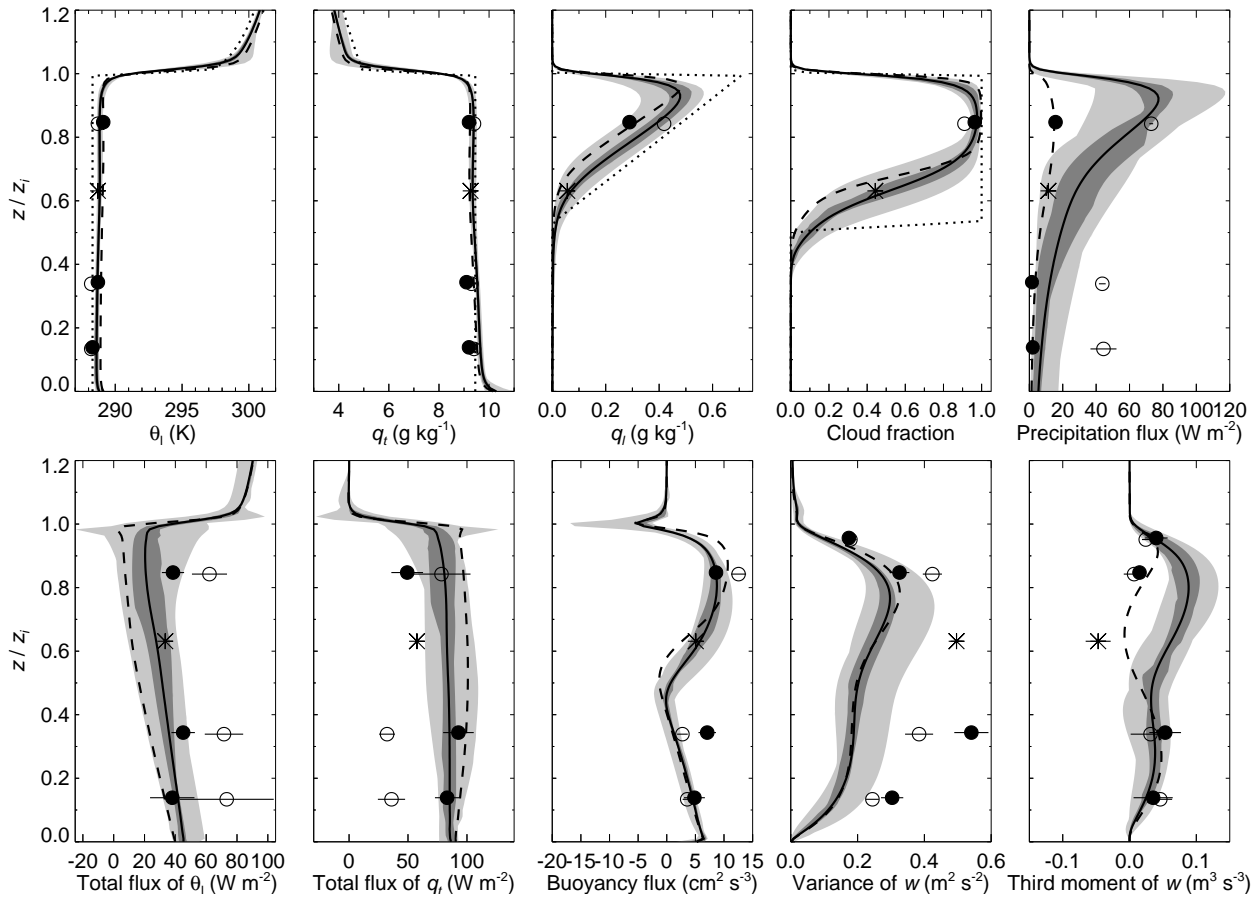


FIG. 3. Ensemble profiles of θ_l , q_t , q_l , cloud fraction (defined in Appendix C), precipitation, total flux of θ_l (including precipitation and radiation), total flux of q_t (including precipitation), buoyancy flux, $\overline{w'^2}$, and $\overline{w'^3}$, all averaged over last four hours of simulations that include cloud-water sedimentation and drizzle. Ensemble range, middle half, and mean denoted by dark and light gray areas, and solid lines. Ensemble mean from simulations that include drizzle but not cloud-water sedimentation denoted by dashed lines. Dotted lines in upper panels denote initial conditions. Measurements shown as open and filled circles for regimes classified as open and closed cells; near cloud base, averages encompass both regimes and are plotted as asterisks because of possible undersampling of open cells at that flight level (vanZanten and Stevens 2005). Horizontal bars are \pm one standard deviation. Vertical axis is altitude normalized by inversion height, in which normalization is first done for each half-hourly profile and then averaged to a uniform grid.

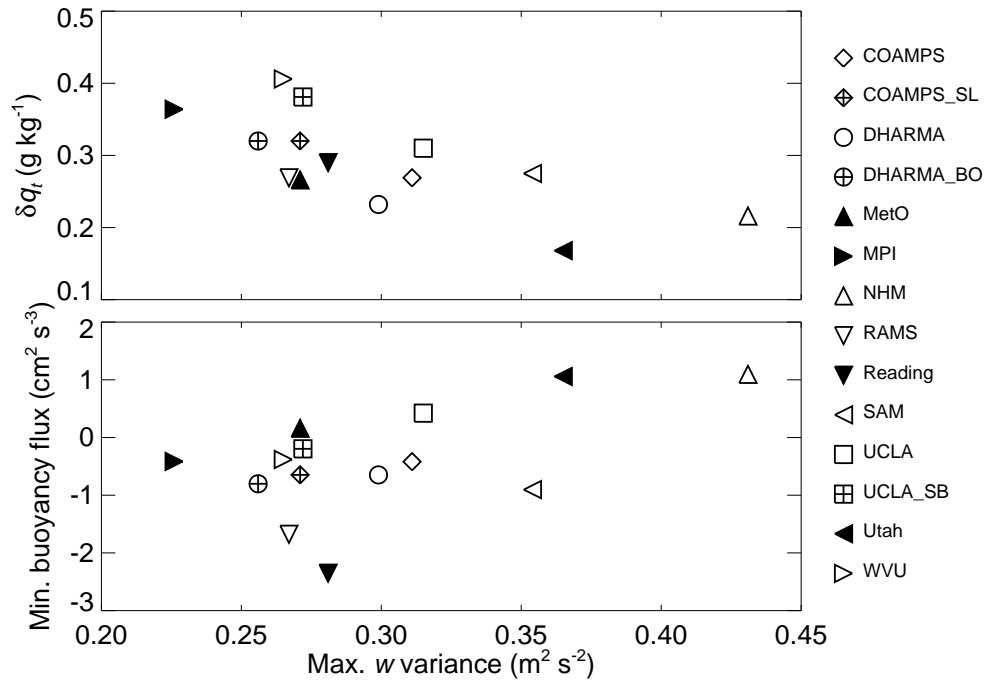


FIG. 4. In-cloud minus below-cloud total water mixing ratio, δq_t , and minimum buoyancy flux near cloud base versus maximum $\overline{w'^2}$, all averaged over last four hours of simulations that include cloud-water sedimentation and drizzle. Diagnostics defined in the text.

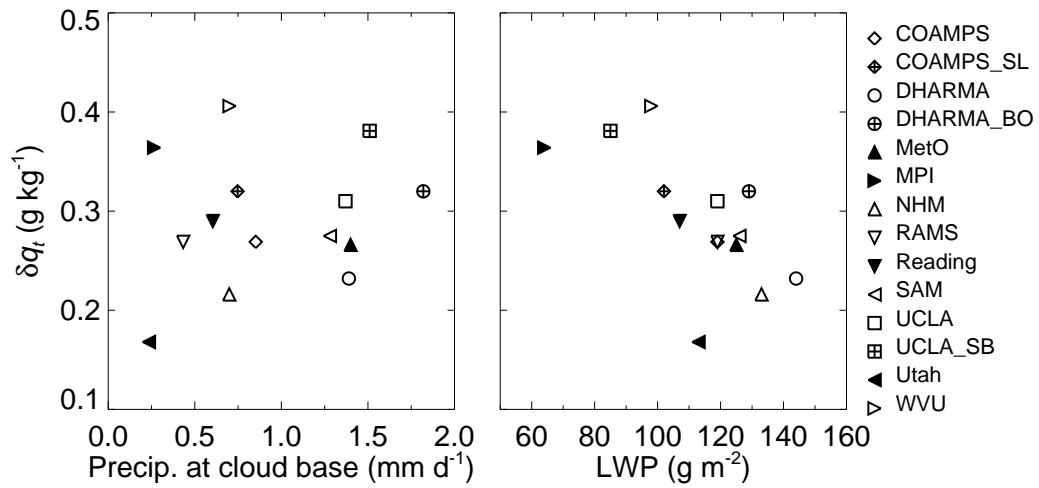


FIG. 5. In-cloud minus below-cloud total water mixing ratio, δq_t (defined in text), versus cloud-base precipitation rate and versus LWP, averaged over last four hours of simulations that include cloud-water sedimentation and drizzle.

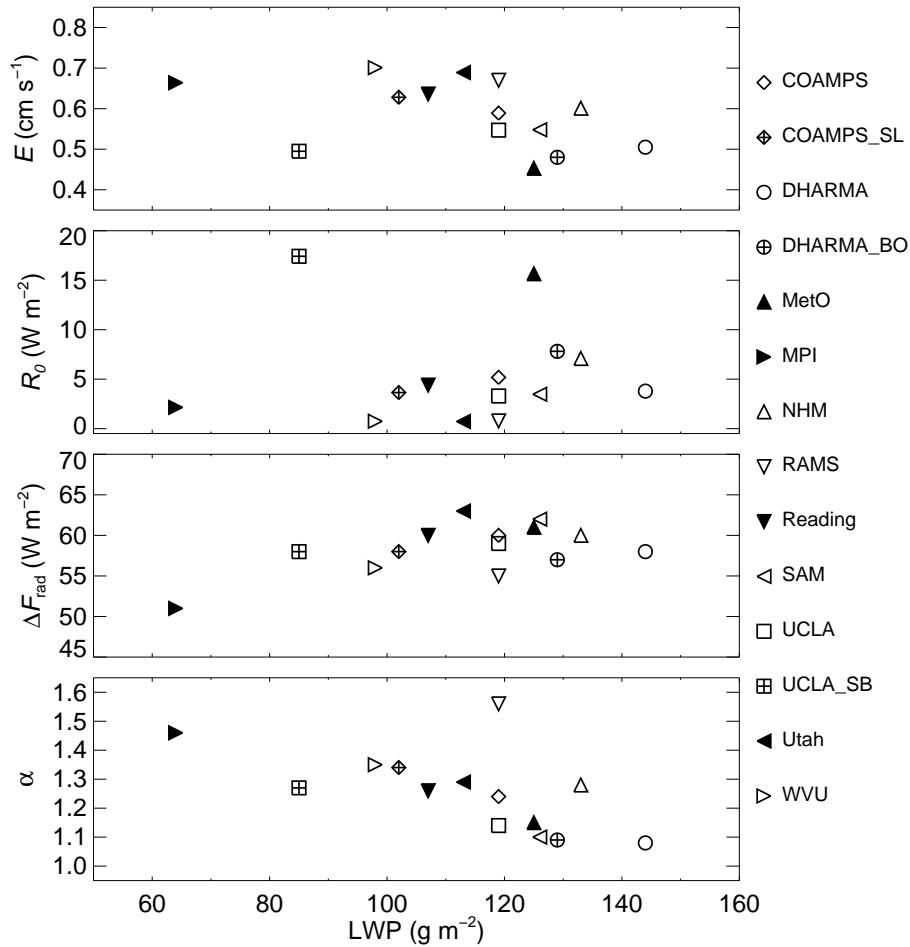


FIG. 6. Terms in mixed-layer heat budget versus LWP, averaged over last four hours of simulations that include cloud-water sedimentation and drizzle: entrainment rate (E), surface precipitation (R_0), longwave cooling (ΔF_{rad}), and ratio of entrainment heat flux plus surface precipitation to longwave cooling (α), all defined in text.

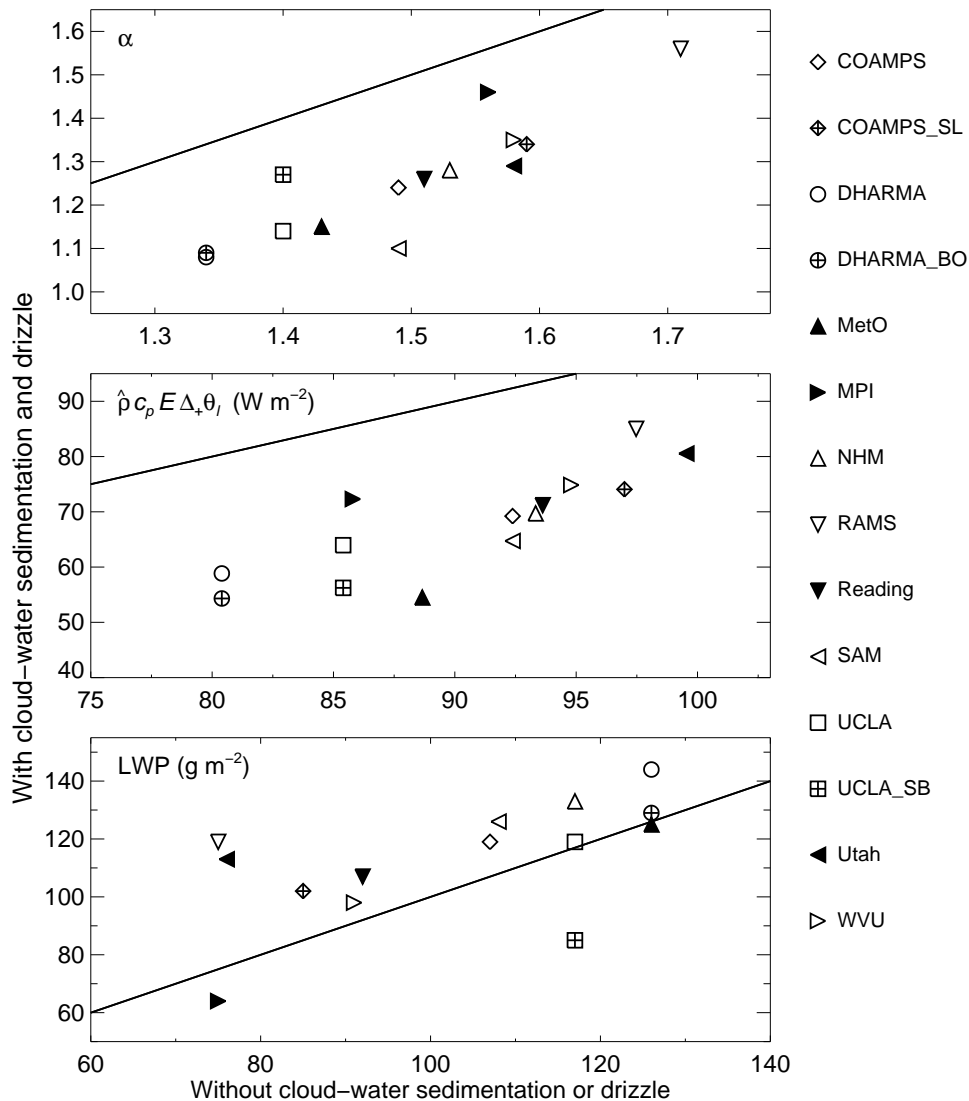


FIG. 7. Ratio of entrainment heating plus surface precipitation to longwave cooling (α , top panel), entrainment heat flux ($\hat{\rho}c_p E \Delta_+ \theta_l$, middle), and LWP (bottom) from simulations that omit both cloud-water sedimentation and drizzle versus those with both processes included. Solid lines denote 1:1 relationships. Entrainment and α computed from mixed-layer budgets. Results averaged over last four hours of simulations.

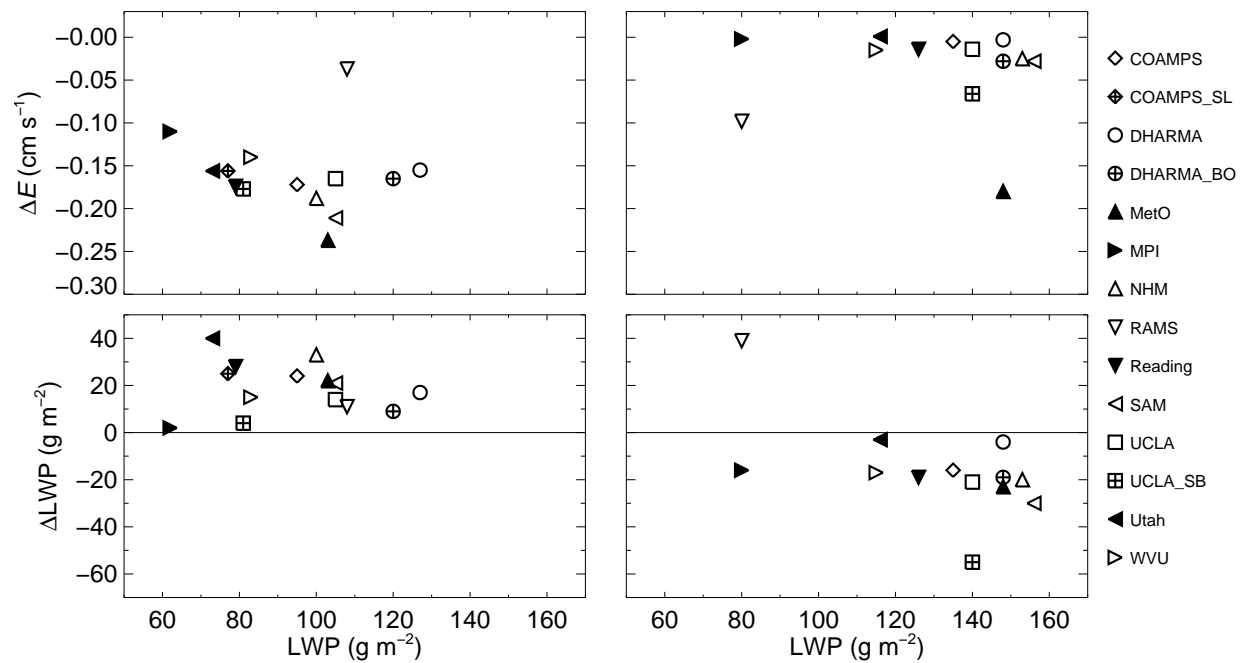


FIG. 8. Change in entrainment rate (top) and LWP (bottom) associated with cloud-water sedimentation (left) and with drizzle (right) averaged over last four hours of simulations. Drizzle is included in simulations on the left, and cloud-water sedimentation is included in simulations on the right. Entrainment rate computed from moisture budget.

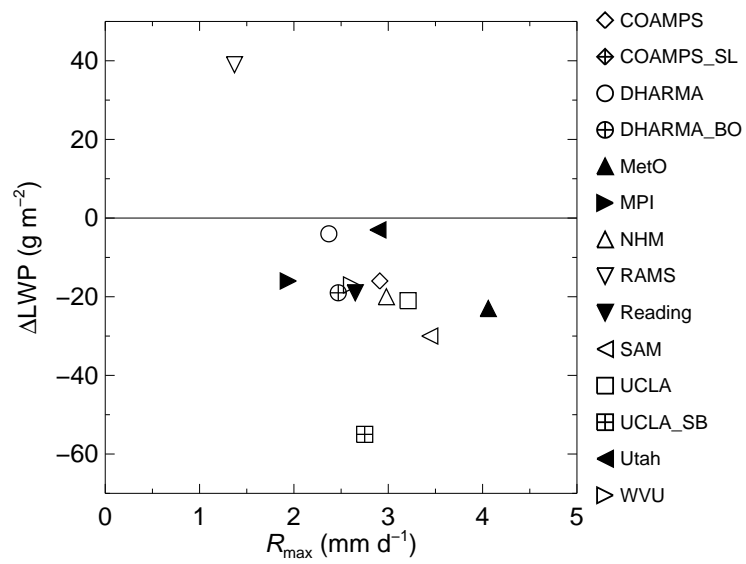


FIG. 9. Peak precipitation in vertical profile (R_{\max}) versus change in LWP associated with drizzle. Cloud-water sedimentation is included, and half-hourly peaks are averaged over last four hours of simulations.

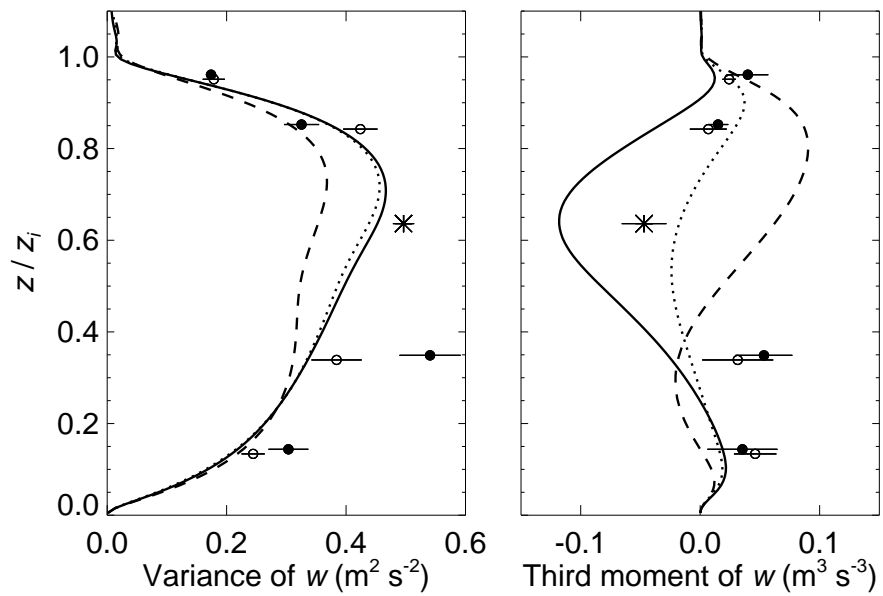


FIG. 10. Second and third moments of the vertical wind averaged over the last four hours of DHARMA simulations without drizzle. Solid lines are results without cloud-water sedimentation, and dotted and dashed lines are results that include cloud-water sedimentation with $\sigma_g = 1.2$ and 1.5 , respectively. Symbols denote measurements, as in Fig. 3.

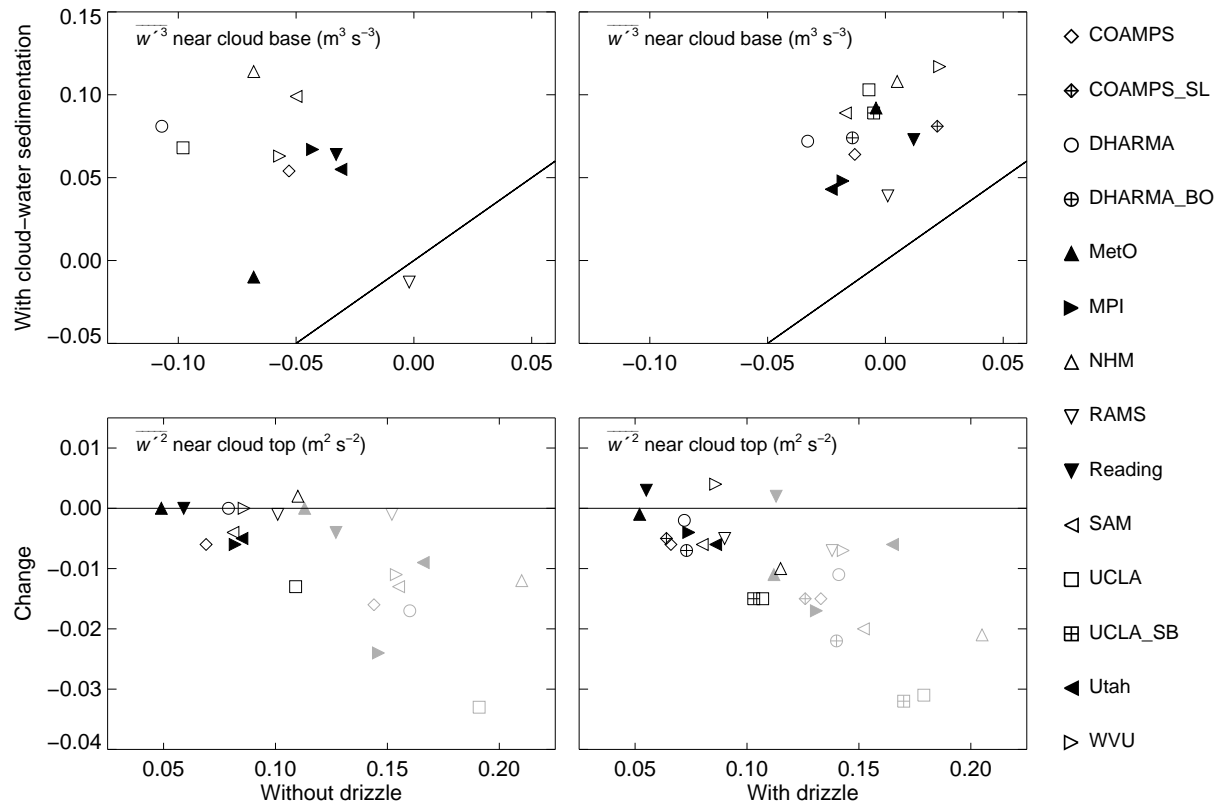


FIG. 11. Third moment of w at $z = 0.7z_i$ from simulations without cloud-water sedimentation versus those that include it (top panels), and change in $\overline{w'^2}$ near cloud top associated with cloud-water sedimentation (bottom panels). Drizzle is omitted in simulations on the left, and included on the right. Solid lines in top panels denote 1:1 relationship; changes in bottom panels taken relative to results without cloud-water sedimentation. Black and grey symbols in bottom panels denote vertical averages over depths 50 and 100 m immediately below z_i , respectively. Results averaged over last four hours of simulations.

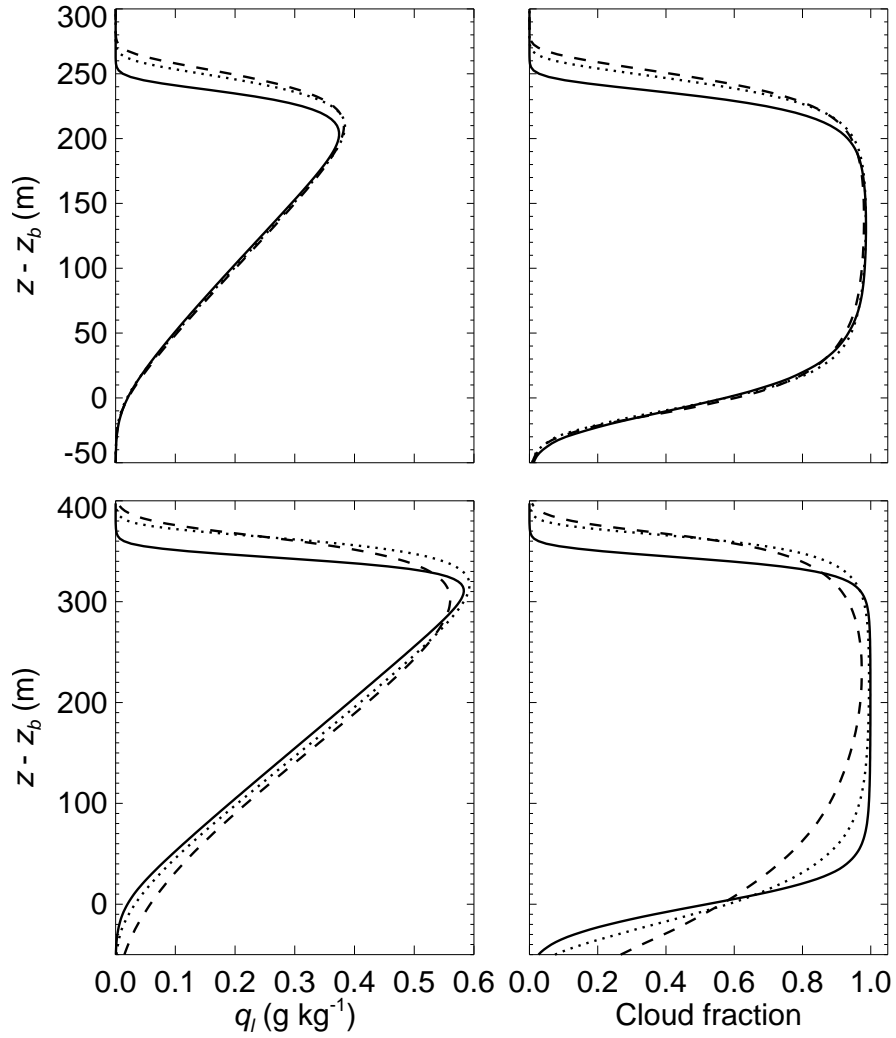


FIG. 12. Profiles of liquid water mixing ratio and cloud fraction averaged over hours 4-6 from DHARMA simulations without drizzle. Top panels are for RF01 and bottom for RF02 conditions. Solid lines are results without cloud-water sedimentation, and dotted and dashed lines are results that include cloud-water sedimentation with $\sigma_g = 1.2$ and 1.5, respectively. Vertical axis is altitude relative to cloud base, recomputed every minute.

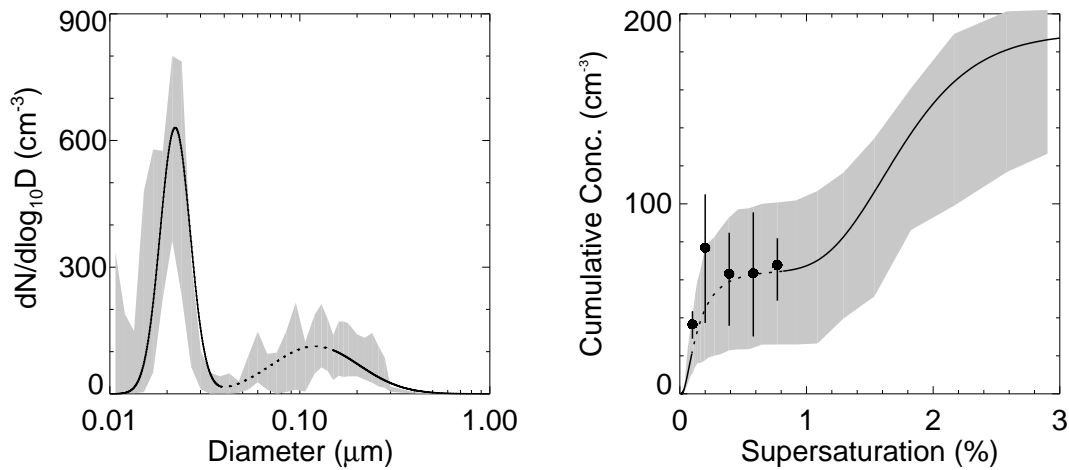


FIG. 13. Differential aerosol size distributions (left) and cumulative CCN spectra (right). Gray shading shows the range of measured aerosol distributions. Data is from the 1330 to 1400 GMT flight segment below cloud. The black curve in the left panel is a subjective fit of the size distribution data; the curve shown in the right panel is the CCN activation spectrum derived from the fitted size distribution and the ammonium bisulfate parameters discussed in the text. The dotted segment of the curves denotes the range of the fit corresponding to the range of CCN-measured supersaturations. Filled circles shown in the right panel are the average CCN measurements and the vertical lines show the range of measured CCN concentrations.

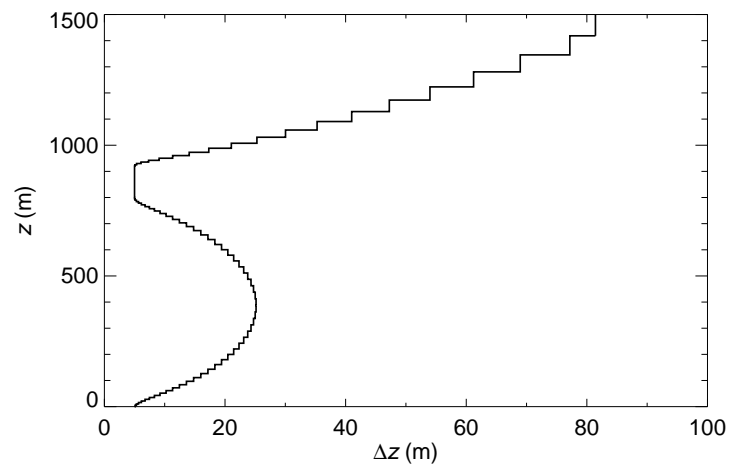


FIG. 14. Vertical grid recommended for all models.

List of Tables

1	Measured droplet concentrations	53
2	Heat budget terms derived from measurements	54
3	List of reported time series	55
4	List of reported profiles	56

TABLE 1. Mean droplet concentration (in units of cm^{-3}) averaged over cloudy segments of horizontal flight legs near cloud top and cloud base, where cloudy air is defined by cloud-droplet concentration exceeding 20 cm^{-3} (from vanZanten and Stevens 2005).

Flight Leg	Open Cells	Closed Cells
Cloud top	56 ± 16	80 ± 17
Cloud base	54 ± 14	60 ± 13

TABLE 2. Heat budget terms (defined in text; fluxes in units of W m^{-2}), derived from measurements, and ensemble medians from averages over last four hours of simulations with drizzle and cloud-water sedimentation. Measurements of entrainment and surface precipitation as in Fig. 1; uncertainties are standard deviations. A 50-m deep inversion layer is assumed both for computing $\Delta_+\theta_l$ in the entrainment heat flux and for additional radiative cooling (using Eq. 5) added to that reported for the boundary layer by vanZanten and Stevens (2005).

Term	Observed	Ensemble Median
$\hat{\rho}c_p E \Delta_+\theta_l$	78 ± 12	69
R_0	10 ± 3.2	3.7
ΔF_{rad}	62 ± 5.0	59
α	1.4 ± 0.16	1.3

TABLE 3. Reported time series, provided at an interval of five minutes or shorter. LWP and precipitation fluxes include all (cloud and rain) condensed water. Cloudy grid cells are defined as those with $N_d > 20 \text{ cm}^{-3}$; cloudy columns are defined as those with of $\text{LWP} > 20 \text{ g m}^{-2}$, a threshold that corresponds to an optical depth of two for cloud-drop effective radius of $15 \text{ }\mu\text{m}$.

Name	Description	Units
time	Time	s
zi	Mean height of $q_t = 8 \text{ g kg}^{-1}$ surface	m
zi_var	Variance of height of $q_t = 8 \text{ g kg}^{-1}$ surface	m^2
zb	Mean height of bottom of lowermost cloudy grid cell	m
zb_var	Variance of height of bottom of lowermost cloudy grid cell	m^2
ndrop_cld	Mean N_d in cloudy grid cells	cm^{-3}
lwp	Mean LWP	g m^{-2}
lwp_var	LWP variance	$\text{g}^2 \text{ m}^{-4}$
cfrac	Fraction of cloudy columns	
tke	$0.5 \int_0^{1.5 \text{ km}} \rho (\overline{u'^2} + \overline{v'^2} + \overline{w'^2}) dz$ (subgrid-scale plus resolved)	kg s^{-2}
wstar	$[2.5 \int_0^{1.5 \text{ km}} (g/\theta_v) \overline{w'\theta'_v} dz]^{1/3}$ (subgrid-scale plus resolved)	m s^{-1}
w2_max	Maximum value of layer-averaged $\overline{w'^2}$	$\text{m}^2 \text{ s}^{-2}$
precip	Mean downward surface precipitation flux	W m^{-2}
precip_var	Variance of downward surface precipitation flux	$\text{W}^2 \text{ m}^{-4}$
precip_max	Maximum downward surface precipitation flux	W m^{-2}

TABLE 4. Horizontally averaged profiles. All variables except for the time and heights, which are independent of time, are comprised of 12 vertical profiles averaged over 30 minute intervals for the duration of the simulations, and one initial profile. Liquid water (e.g., in q_l and θ_l) includes all (cloud and rain) condensed water. Cloudy grid cells are defined as those with $N_d > 20 \text{ cm}^{-3}$. Rainwater is defined by drops $> 25 \text{ }\mu\text{m}$ radius for bin microphysics models.

Name	Description	Units
time	End of averaging interval	s
zt	Altitude of layer mid-points	m
zw	Altitude of layer boundaries	m
rho	Reference air density	kg m^{-3}
u	Zonal wind	m s^{-1}
v	Meridional wind	m s^{-1}
thetal	Liquid water potential temperature	K
qt	Total water (vapor plus liquid) mixing ratio	g kg^{-1}
ql	Liquid water mixing ratio	g kg^{-1}
qr	Rainwater mixing ratio	g kg^{-1}
cfrac	Fraction of cloudy grid cells	
ndrop_cld	Mean N_d in cloudy grid cells	cm^{-3}
ss	Mean supersaturation	%
u_var	Resolved $\overline{u'^2}$	$\text{m}^2 \text{ s}^{-2}$
v_var	Resolved $\overline{v'^2}$	$\text{m}^2 \text{ s}^{-2}$
w_var	Resolved $\overline{w'^2}$	$\text{m}^2 \text{ s}^{-2}$
w_skw	Resolved $\overline{w'^3}$	$\text{m}^3 \text{ s}^{-3}$
thetal_var	Resolved $\overline{\theta_l'^2}$	K^2
qt_var	Resolved $\overline{q_t'^2}$	$\text{g}^2 \text{ kg}^{-2}$
ql_var	Resolved $\overline{q_l'^2}$	$\text{g}^2 \text{ kg}^{-2}$
rad_flux	Net radiative flux	W m^{-2}
precip	Precipitation flux (positive downward)	W m^{-2}
tot_tw	Total θ_l flux, including subgrid-scale and precipitation	W m^{-2}
sgs_tw	Subgrid-scale θ_l flux	W m^{-2}
tot_qw	Total q_t flux, including subgrid-scale and precipitation	W m^{-2}
sgs_qw	Subgrid-scale q_t flux	W m^{-2}
tot_uw	Total (subgrid-scale plus resolved) zonal momentum flux	$\text{kg m}^{-1} \text{ s}^{-2}$
sgs_uw	Subgrid-scale zonal momentum flux	$\text{kg m}^{-1} \text{ s}^{-2}$
tot_vw	Total (subgrid-scale plus resolved) meridional momentum flux	$\text{kg m}^{-1} \text{ s}^{-2}$
sgs_vw	Subgrid-scale meridional momentum flux	$\text{kg m}^{-1} \text{ s}^{-2}$
sgs_pr	Subgrid-scale Prandtl number	
sgs_tke	Subgrid-scale TKE	$\text{m}^2 \text{ s}^{-2}$
tot_boy	Total (subgrid-scale plus resolved) buoyancy TKE production	$\text{m}^2 \text{ s}^{-3}$
sgs_boy	Subgrid-scale buoyancy TKE production	$\text{m}^2 \text{ s}^{-3}$
tot_shr	Total (subgrid-scale plus resolved) shear TKE production	$\text{m}^2 \text{ s}^{-3}$
transport	Resolved TKE transport (turbulent plus pressure)	$\text{m}^2 \text{ s}^{-3}$
dissipation	TKE dissipation (explicit plus numerical)	$\text{m}^2 \text{ s}^{-3}$